Supporting Information

Elucidating activity-property relationships of dual catalysts for polyethylene terephthalate depolymerisation

Matt J. Price,[a] Anna Bachs Herrera,[b,c] Arianna Brandolese,[a] Yuya Watanabe,[a] Matthew N. Grayson,[b*] Antoine Buchard,[c*] and Andrew P. Dove[a*]

[a]*School of Chemistry University of Birmingham Edgbaston, Birmingham, B15 2TT, United Kingdom*

[b]*Department of Chemistry, University of Bath, Claverton Down, Bath, BA2 7AY, UK*

[c]*Department of Chemistry, Green Chemistry Centre of Excellence, University of York, York, YO10 5DD, United Kingdom*

**Correspondence: a.dove@bham.ac.uk*

Table of Contents

General information

All chemicals were commercially available (purchased from Sigma-Aldrich) and used without further purification (unless otherwise stated). All the metal acetates were purchased in their hydrated forms: zinc acetate dihydrate, manganese(II) acetate tetrahydrate, magnesium (II) acetate tetrahydrate, lanthanum acetate hydrate. PET was purchased from Goodfellow Cambridge Limited and used in the form of white pellets in all experiments (pellet size: 3 − 5 mm). 1-Methyl-2-pyrrolidinone was purified by distillation under vacuum using a Schlenk line.

All NMR spectroscopy experiments were performed at 25 °C on a Bruker DPX-300/400 NMR instrument operating at 300 or 400 MHz for ^{1}H (100.57 MHz for ^{13}C). ^{1}H NMR spectra are referenced to residual proton solvent (δ_H = 2.50 for DMSO-d_6 and δ_H = 7.26 for $CDCl_3$). The resonance multiplicities are described as s (singlet), d (doublet), t (triplet), q (quartet) or m (multiplet).

General depolymerisation protocol of PET by Dual Catalysis

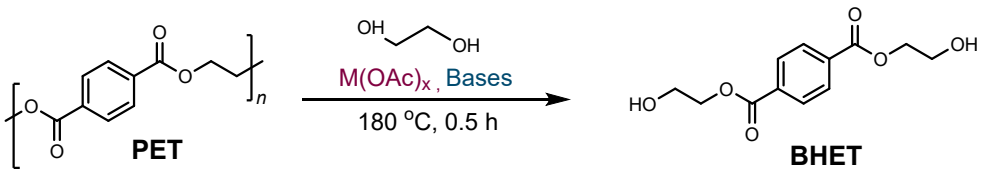

Scheme S1. Generic scheme of PET glycolysis by dual catalysts.

A 20 mL scintillation vial was charged with ethylene glycol (2.8 mL, 3120 mg, 50 mmol, 20 equiv.), metal acetate hydrate (0.025-0.25 mmol, 0.01-0.10 equiv.), base (0.025-0.25 mmol, 0.01-0.10 equiv.) and *N*-methyl-pyrrolidone (0.024 mL, 25 mg, 0.25 mmol, 0.10 equiv.) and sealed with a screw cap. The mixture was brought to 180 °C. PET (480 mg, 2.5 mmol, 1 equiv.) was added to the solution and stirred at this temperature for 0.5 h. Aliquots of 0.1 mL were taken at regular timepoints and prepared for ^{1}H NMR spectroscopic analysis in DMSO-d_6. Once all the PET had been depolymerised, water (15 mL) was added to the solution and cooled to 4 °C for 18 h, and the resulting crystals of bis(2-hydroxyethylene)terephthalate (BHET) (561 mg, 2.4 mmol, 96%) were recovered by vacuum filtration, washing with cold water (5 mL) and drying under reduced pressure before being analysed by ^{1}H NMR spectroscopy.[1]

For those mixtures with paramagnetic catalysts ($Mn(OAc)_2$), each sample was filtered over silica to remove the metal acetate catalyst; this was also performed on a non-paramagnetic sample to verify the process did not alter the monomer amounts.

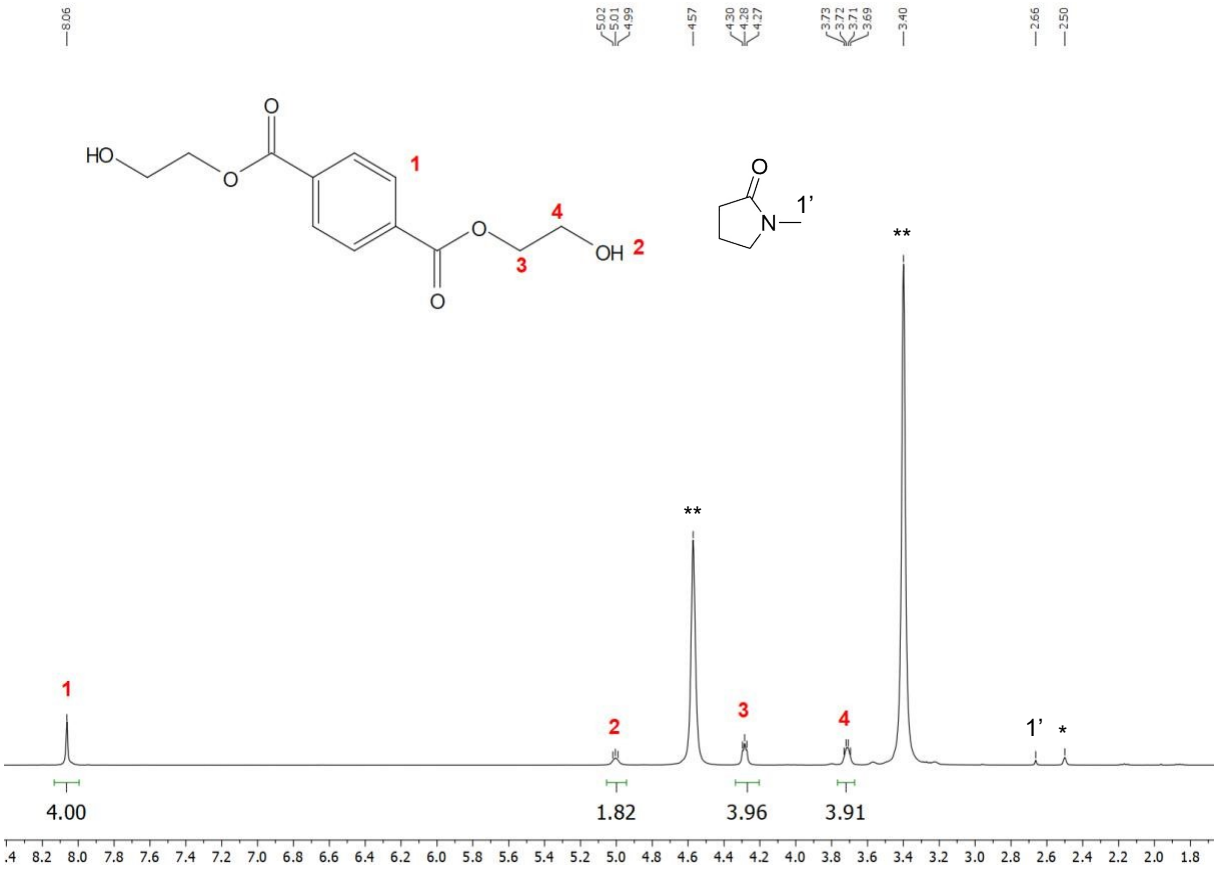
8.06
5.02
5.01
4.99
4.57
4.30
4.28
4.27
3.73
3.72
3.71
3.69
3.40
2.66
2.50
HO
O
O
O
O
OH
1
2
3
4
O
N
1'
**
**
1
2
3
4
1'
*
4.00
1.82
3.96
3.91

aliquot. * = DMSO; ** = EG

Table S1. Metal acetates chosen and their physicochemical properties, where χ = electronegativity.

Metal ion	Pauling χ	Gagné-Hawthorne Parameter / Å	Shannon-Prewitt Ionic Radius (6-valent) / Å	Pearson Hardness / eV
Zinc(II)	1.65	0.405	0.740	4.94
Magnesium(II)	1.31	0.337	0.720	3.90
Manganese(III)	1.55	0.513	0.645	3.72
Lanthanum(III)	1.10	0.343	1.032	2.60
Scandium(III)	1.36	n.a.	0.745	3.34

Table S2. Table comparing the initial reaction rate for the dual and single catalyst systems.

Base	Metal	Rate
DMA	/	0.00127±0.00008
Im	/	0.00041±0.00002
NMI	/	0.00024±0.00002
DABCO	/	0.00113±0.00012
DMAP	/	0.00143±0.00017
ABCO	/	0.00237±0.00005
DBU	/	0.0116±0.0016
/	$Zn(OAc)_2$	0.0202±0.0013
DMA	$Zn(OAc)_2$	0.0316±0.0012
Im	$Zn(OAc)_2$	0.0416±0.0014
NMI	$Zn(OAc)_2$	0.0308±0.0010
DABCO	$Zn(OAc)_2$	0.0199±0.0013
DMAP	$Zn(OAc)_2$	0.0249±0.0007
ABCO	$Zn(OAc)_2$	0.0238±0.0006
DBU	$Zn(OAc)_2$	0.0415±0.0019
/	$Mg(OAc)_2$	0.0358±0.0010
DMA	$Mg(OAc)_2$	0.0369±0.0040
Im	$Mg(OAc)_2$	0.0343±0.0013
NMI	$Mg(OAc)_2$	0.0349±0.0014
DABCO	$Mg(OAc)_2$	0.0376±0.0028

DMAP	$Mg(OAc)_2$	0.0413±0.0011
ABCO	$Mg(OAc)_2$	0.0523±0.0030
DBU	$Mg(OAc)_2$	0.0470±0.0030
/	$Mn(OAc)_2$	0.0443±0.0010
DMA	$Mn(OAc)_2$	0.0501±0.0040
Im	$Mn(OAc)_2$	0.0399±0.0017
NMI	$Mn(OAc)_2$	0.0591±0.0040
DABCO	$Mn(OAc)_2$	0.0373±0.0008
DMAP	$Mn(OAc)_2$	0.0316±0.0006
ABCO	$Mn(OAc)_2$	0.0335±0.0004
DBU	$Mn(OAc)_2$	0.0320±0.0009
/	$La(OAc)_3$	0.0241±0.0006
DMA	$La(OAc)_3$	0.0233±0.0003
Im	$La(OAc)_3$	0.0272±0.0006
NMI	$La(OAc)_3$	0.0288±0.0007
DABCO	$La(OAc)_3$	0.0271±0.0004
DMAP	$La(OAc)_3$	0.0235±0.0005
ABCO	$La(OAc)_3$	0.0320±0.0008
DBU	$La(OAc)_3$	0.0411±0.0020

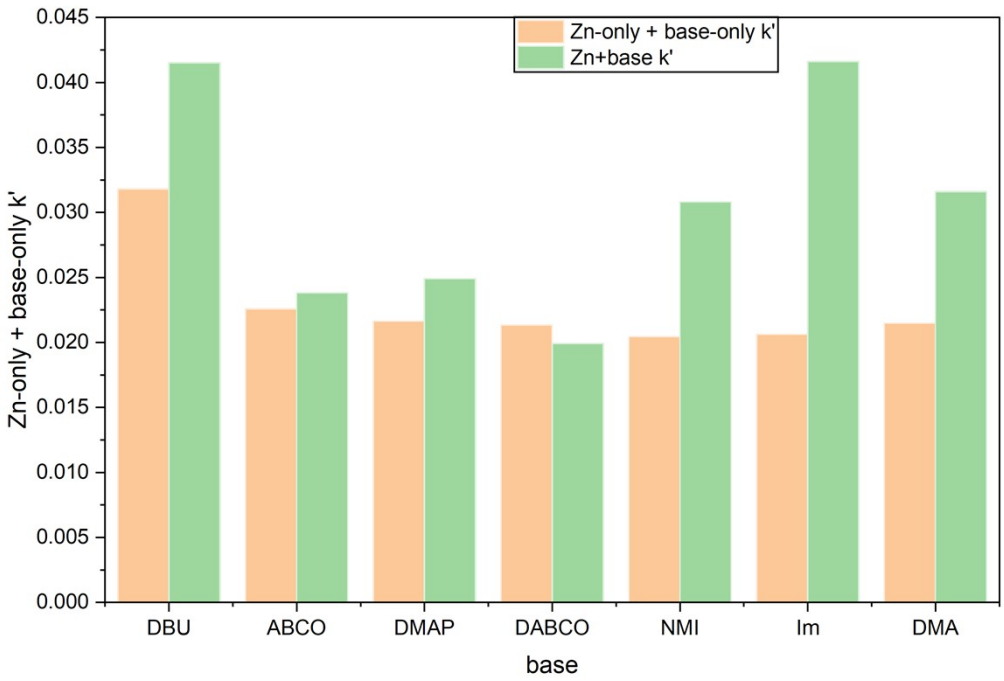

Fig. S2. Bar chart showing that the dual catalyst systems outperform the single catalyst system when $Zn(OAc)_2$ is used.

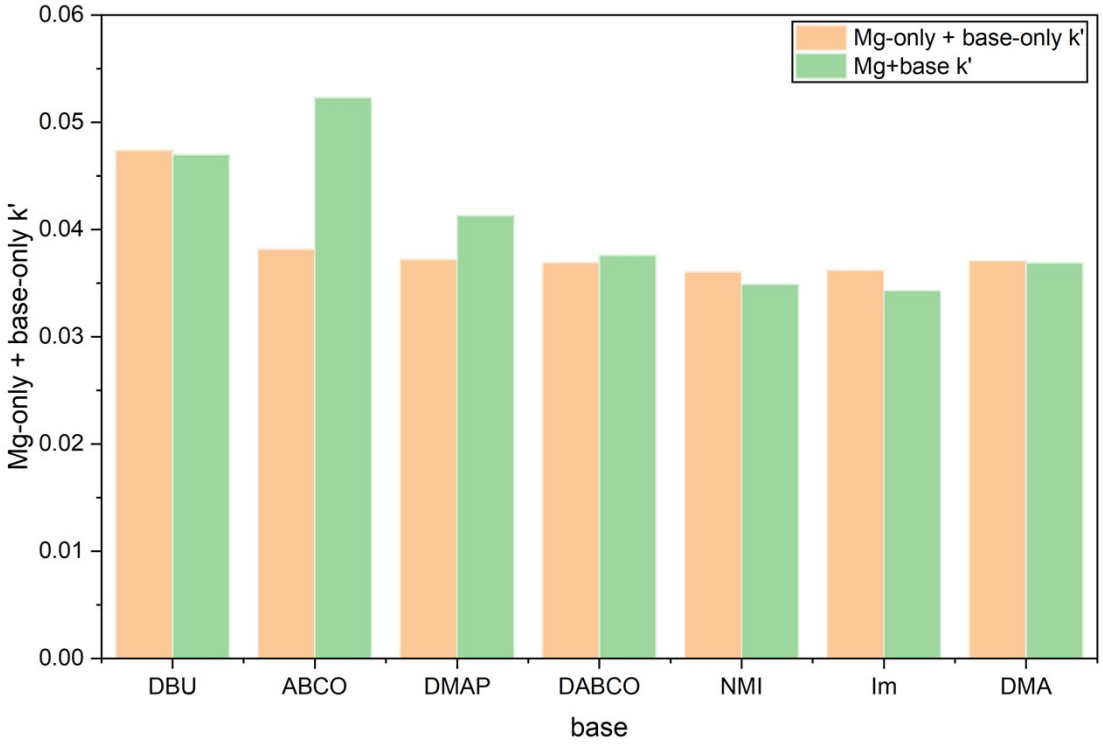

Fig. S3. Bar chart showing that the dual catalyst systems outperform the single catalyst system when $Mg(OAc)_2$ is used.

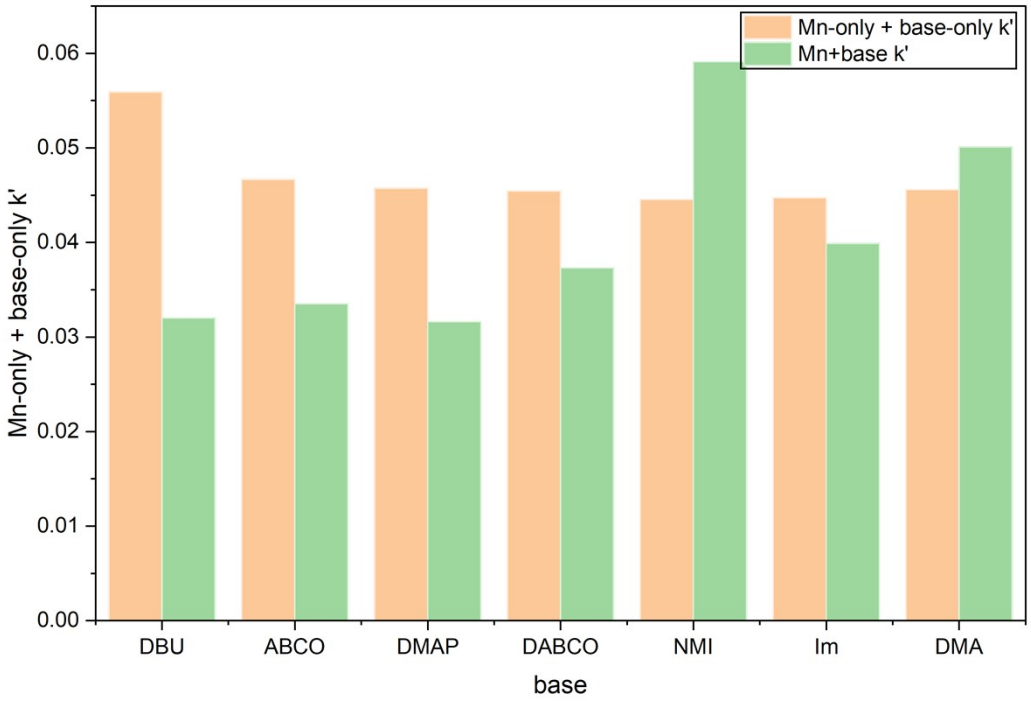

Fig. S4. Bar chart showing that the dual catalyst systems outperform the single catalyst system when $Mn(OAc)_2$ is used.

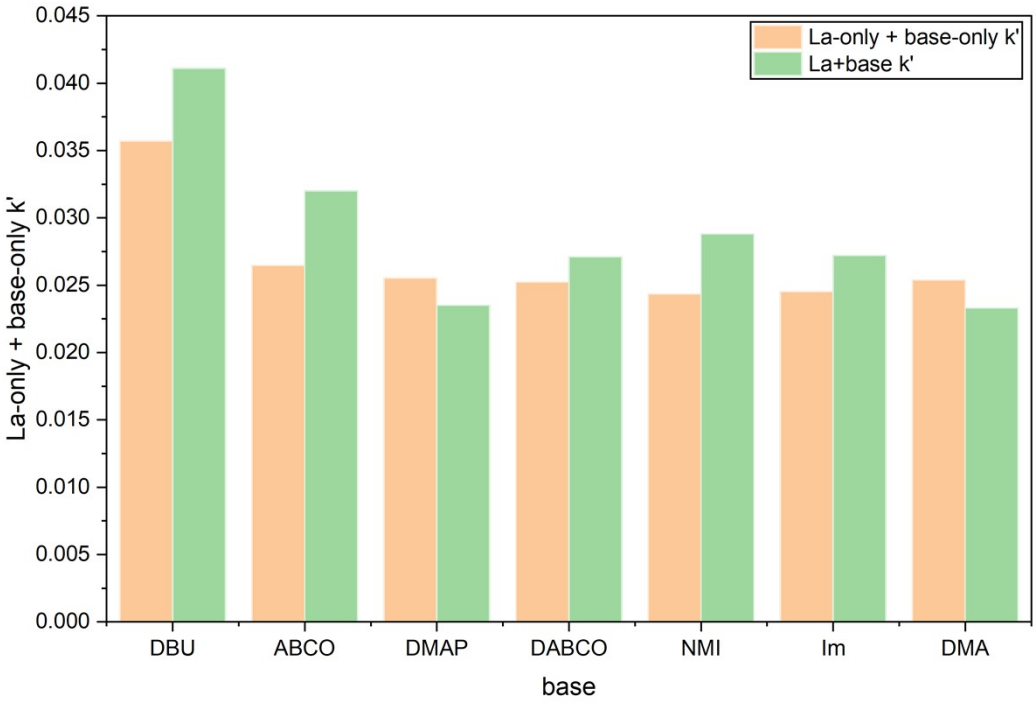

Fig. S5. Bar chart showing that the dual catalyst systems outperform the single catalyst system when $La(OAc)_3$ is used.

Metal Acetate Standalone Catalysis

A model of PET degradation uses surface area calculations to determine the rate of degradation and culminates in Equation S1 below, where *C* is the BHET NMR yield. This model is a surface-only mediated process, so it can be assumed that any catalyst for which kinetic data fits this model proceeds *via* a surface-only degradation pattern

$$1 - (1 - C)^{2/3} = k't \qquad \textbf{(Equation S1)}$$

For each catalyst combination, *k*' was derived from the pseudo-first-order rate constant (and therefore activity).[2]

The Lewis Acids were screened both to determine relationships with activity as well as to provide controls for the activity of the dual catalysts. They were screened as standalone PET glycolysis catalysts at 1 mol% loading (with respect to PET repeat unit).

Table S3. Metal acetate-only catalysed glycolysis first-order rate constants *k*'.

Metal Acetate	***k'*** **/ min^{-1}**
$Zn(OAc)_2$	0.0202±0.0013
$Mg(OAc)_2$	0.0358±0.0010
$Mn(OAc)_2$	0.0443±0.0010
$La(OAc)_3$	0.0241±0.0006

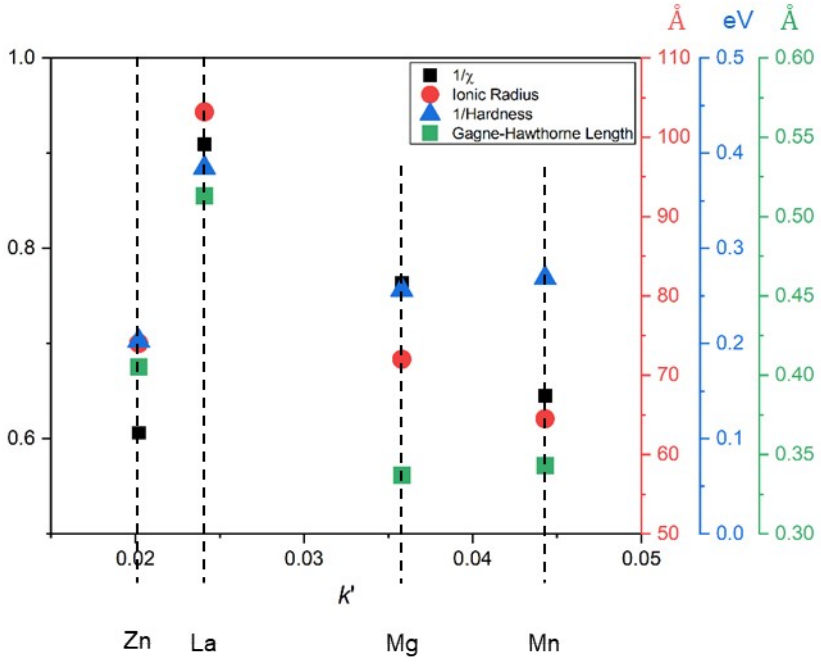

Fig.S6. Scatter plot of shown physicochemical properties (Pauling χ; Gagné-Hawthorne Parameter/ Å; Ionic Radius/ Å; Pearson Hardness/ eV) with respect to the first-order rate constant *k*' of the metal acetate-catalysed glycolysis reaction.

Base Standalone Catalysis

Bases were screened both to determine relationships with activity as well as to provide controls for the activity of the dual catalysts. They were screened as standalone PET glycolysis catalysts at 1 mol% loading (with respect to PET repeat unit).

Table S4. Base-only catalysed glycolysis first-order rate constants *k*'.

Base	p*Ka*H (in water)	*k*' / min^{-1}	Adjusted R^2
DMA	5.0	0.00127±0.00008	0.992
Im	7.0	0.00041±0.00002	0.978
NMI	7.4	0.00024±0.00002	0.971
DABCO	8.8	0.00113±0.00012	0.922
DMAP	9.6	0.00143±0.00017	0.909
ABCO	11.0	0.00237±0.00005	0.997
DBU	13.5	0.0116±0.0016	0.878

The activity of base-only catalysed PET glycolysis correlated strongly with basicity, in an exponential function in the case of *k*' (Fig.S3).

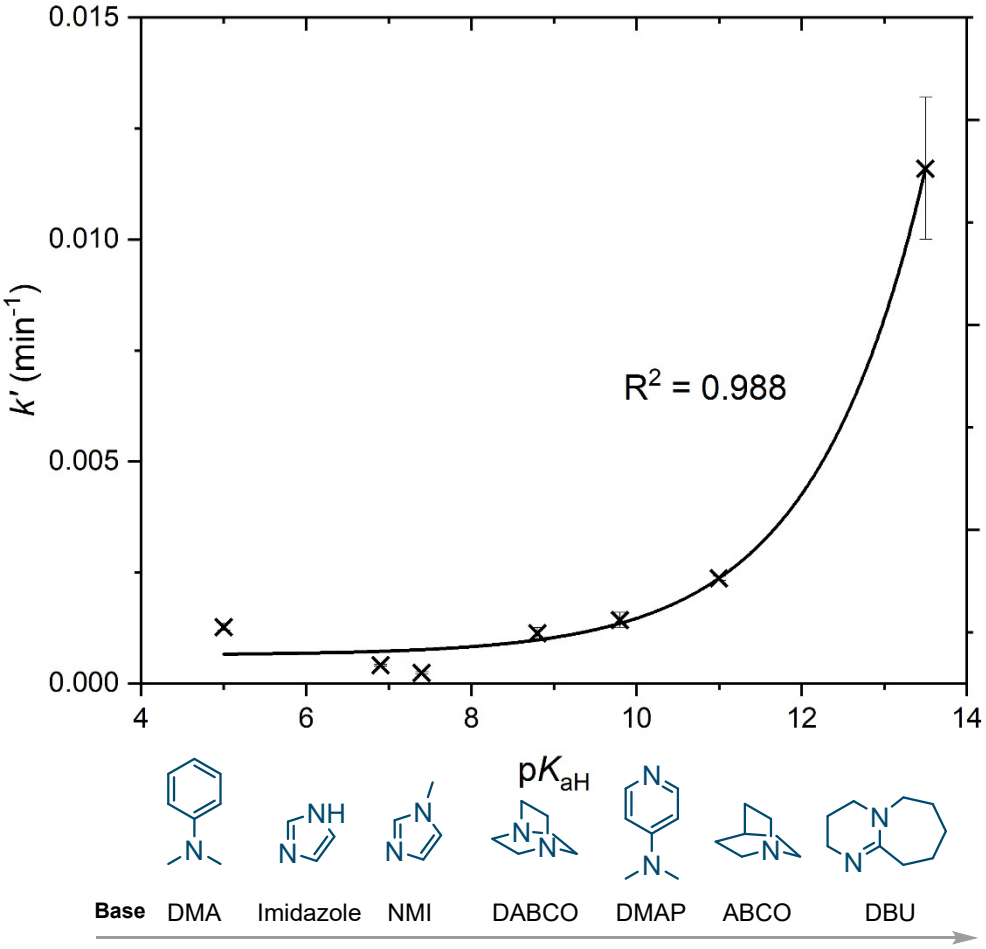

Fig.S7. Pseudo-first-order rate constants (*k'*) of standalone base-catalysed PET glycolysis *versus* p*Ka*H.

Metal Acetate / Base Dual Catalyst Kinetics

The catalyst combinations were screened at 1 mol% following the general depolymerisation protocol.

The initial values of *k*' were derived from the conversion-time plots and were calculated for each combination of metal acetate and base, so that the values of R^2 were maximised for each gradient calculation (Tables S4-S7). These values of *k*' were then compared to gain a greater understanding of the relationship between properties such as basicity and activity in metal-base dual catalysts.

Table S5. Range of bases used in the study, and their *k*' and R^2 values for $Zn(OAc)_2$.

Base	*k*' / min^{-1}	Adjusted R^2
DMA	0.0316±0.0012	0.992
Im	0.0416±0.0014	0.994
NMI	0.0308±0.0010	0.992
DABCO	0.0199±0.0013	0.970
DMAP	0.0249±0.0007	0.995
ABCO	0.0238±0.0006	0.995
DBU	0.0415±0.0019	0.989

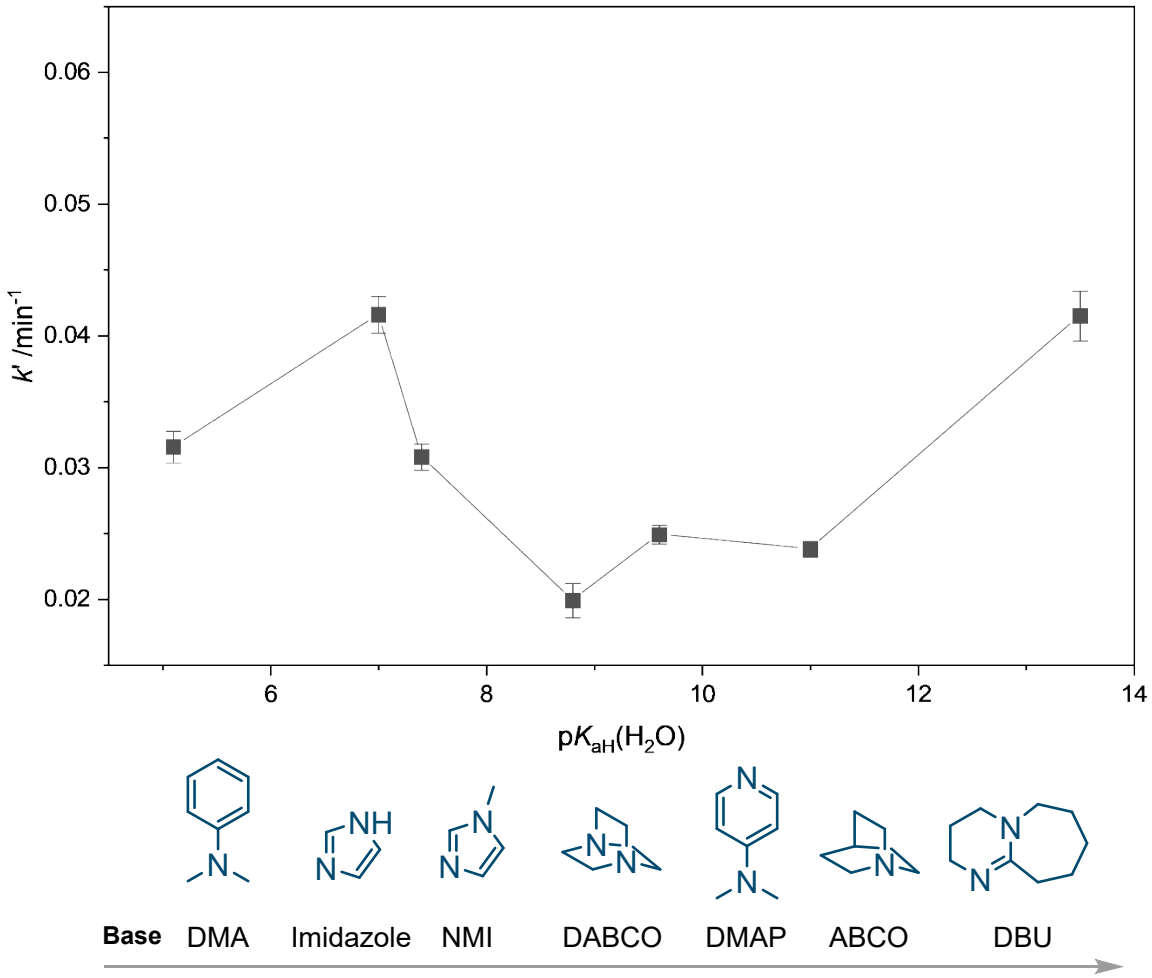

Fig.S8. Values of *k*' PET glycolysis catalysed by $Zn(OAc)_2$ / base combinations.

Table S6. Range of bases used in the study, and their *k*' and R^2 values for $Mg(OAc)_2$.

Base	*k*' / min^{-1}	Adjusted R^2
DMA	0.0369±0.0040	0.941
Im	0.0343±0.0013	0.993
NMI	0.0349±0.0014	0.992
DABCO	0.0376±0.0028	0.967
DMAP	0.0413±0.0011	0.990
ABCO	0.0523±0.0030	0.972
DBU	0.0470±0.0030	0.962

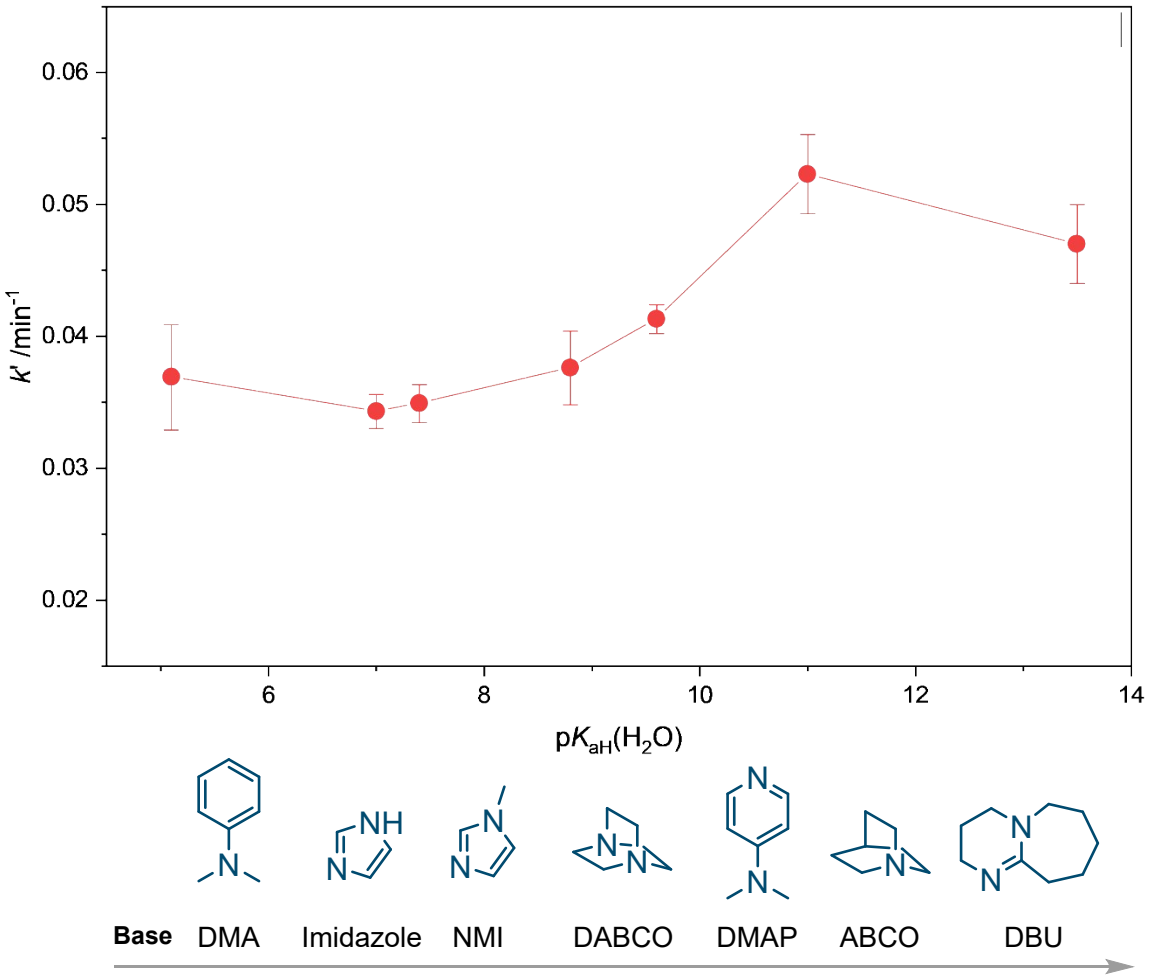

Fig.S9. Values of *k*' PET glycolysis catalysed by $Mg(OAc)_2$ / base combinations.

Table S7. Range of bases used in the study, and their *k*' and R^2 values for $La(OAc)_3$.

Base	*k*' / min^{-1}	Adjusted R^2
DMA	0.0233±0.0003	0.997
Im	0.0272±0.0006	0.998
NMI	0.0288±0.0007	0.996
DABCO	0.0271±0.0004	0.996
DMAP	0.0235±0.0005	0.997
ABCO	0.0320±0.0008	0.997
DBU	0.0411±0.0020	0.984

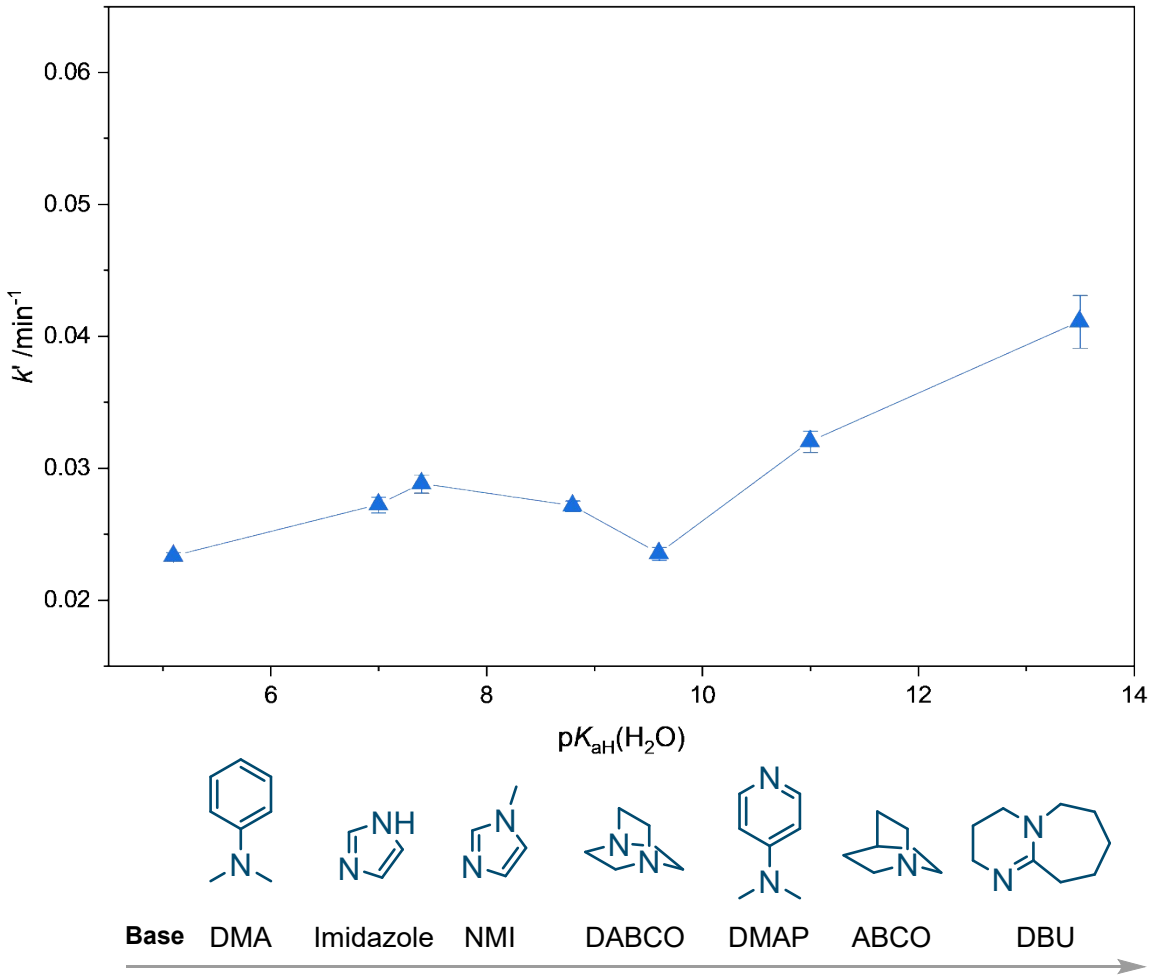

Fig.S10. Values of *k*' PET glycolysis catalysed by $La(OAc)_3$ / base combinations.

Table S8. Range of bases used in the study, and their *k*' and R^2 values for $Mn(OAc)_2$.

Base	*k*' / min^{-1}	Adjusted R^2
DMA	0.0501±0.0040	0.945
Im	0.0399±0.0017	0.946
NMI	0.0591±0.0040	0.951
DABCO	0.0373±0.0008	0.998
DMAP	0.0316±0.0006	0.998
ABCO	0.0335±0.0004	0.999
DBU	0.0320±0.0009	0.996

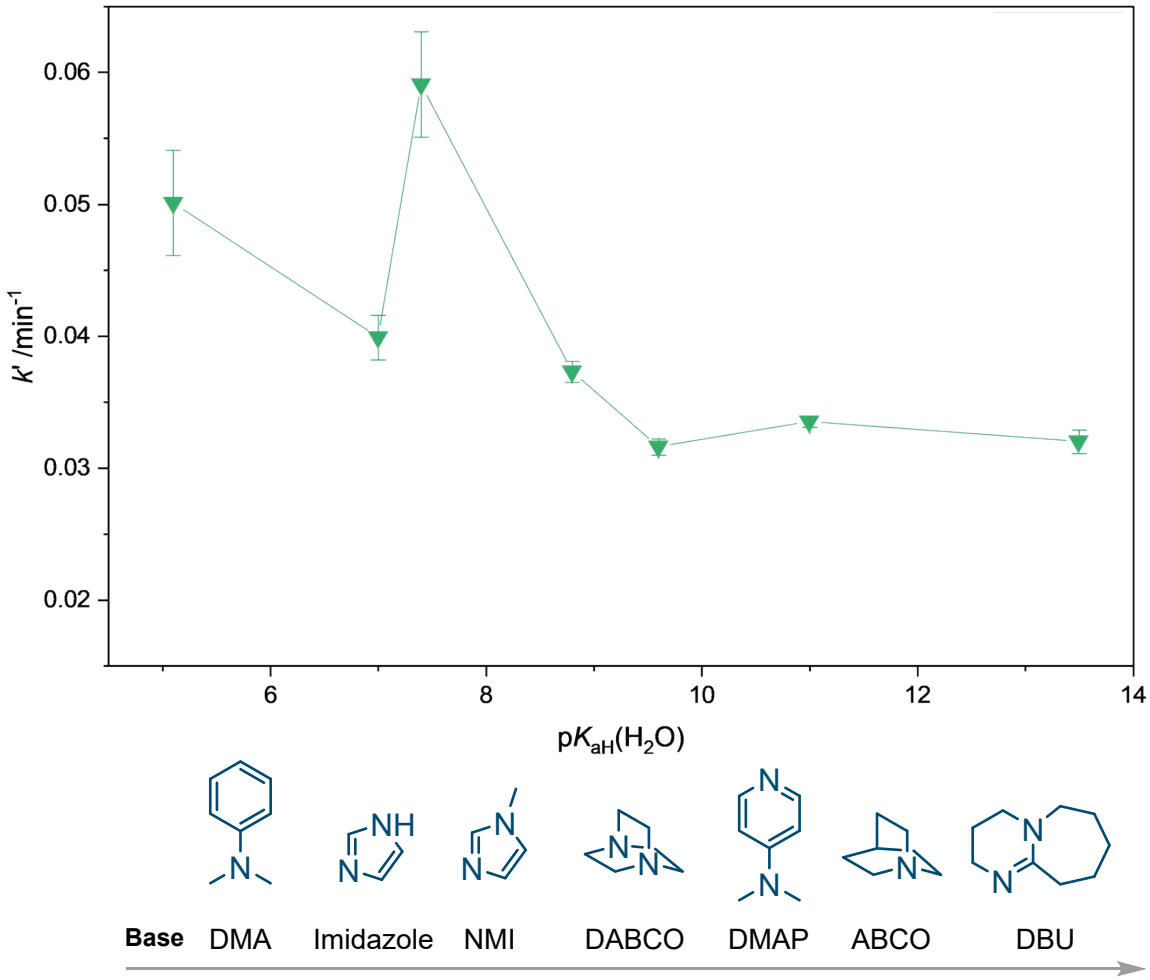

Fig.S11. Values of *k*' PET glycolysis catalysed by $Mn(OAc)_2$ / base combinations.

Table S9. *p*KaHs values in acetonitrile (MeCN).

Base	*p*KaH in MeCN	Source
DMA	11.43	2
Im	11.47	2
NMI	11.90	2
ABCO	19.70	2
DMAP	17.95	1
DABCO	18.29	2
DABCO	18.80	1
DBU	24.34	2

1. Baidya M. *et al*, *Org. Biomol. Chem*., **2010**, *8*, 1929-1935 ; 2. Tshepelevitsh, S. *et al.*, *Eur. J. Org. Chem*., **2019**, 6735-6748.

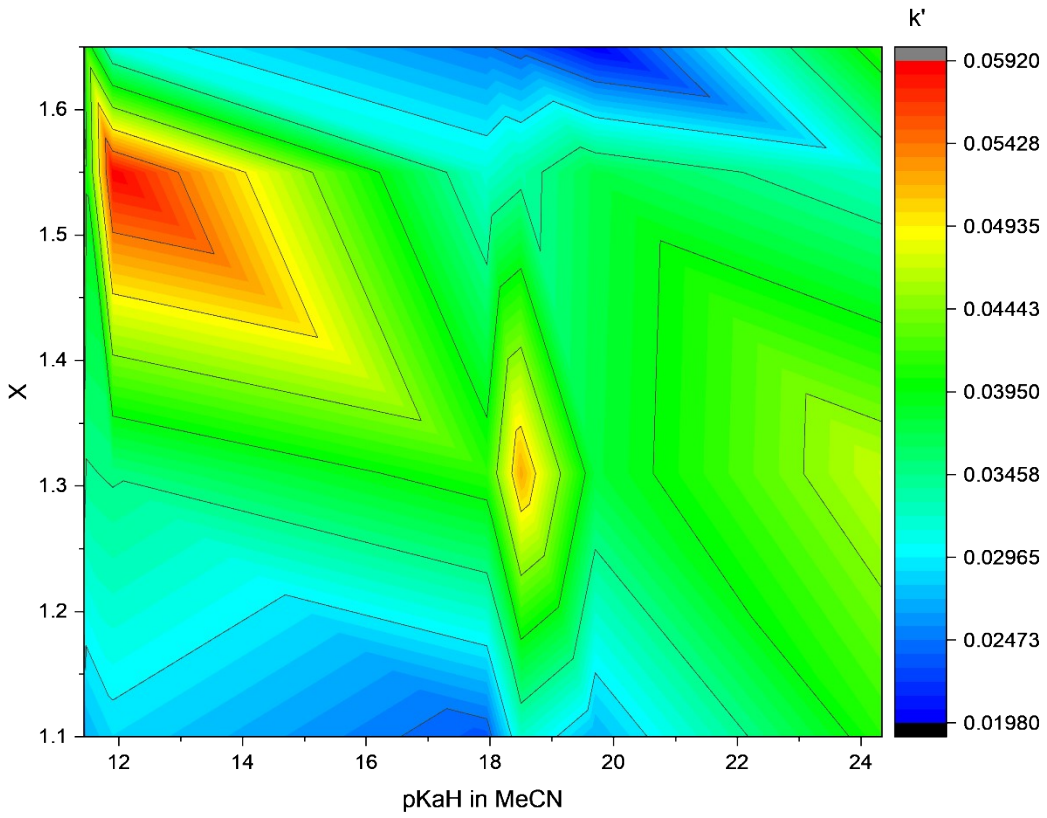

Fig. S12. Heat map showing the correlation between rate constants (k`, min-1) for the metal acetate-base combinations, the pKaH of the bases in MeCN and the electronegativity of the metal acetates on the x and y axes, respectively.

Additional Catalyst Studies

The following catalyst control studies were conducted to rule out any potential coordination of ethylene glycol and NMP to $Zn(OAc)_2$.

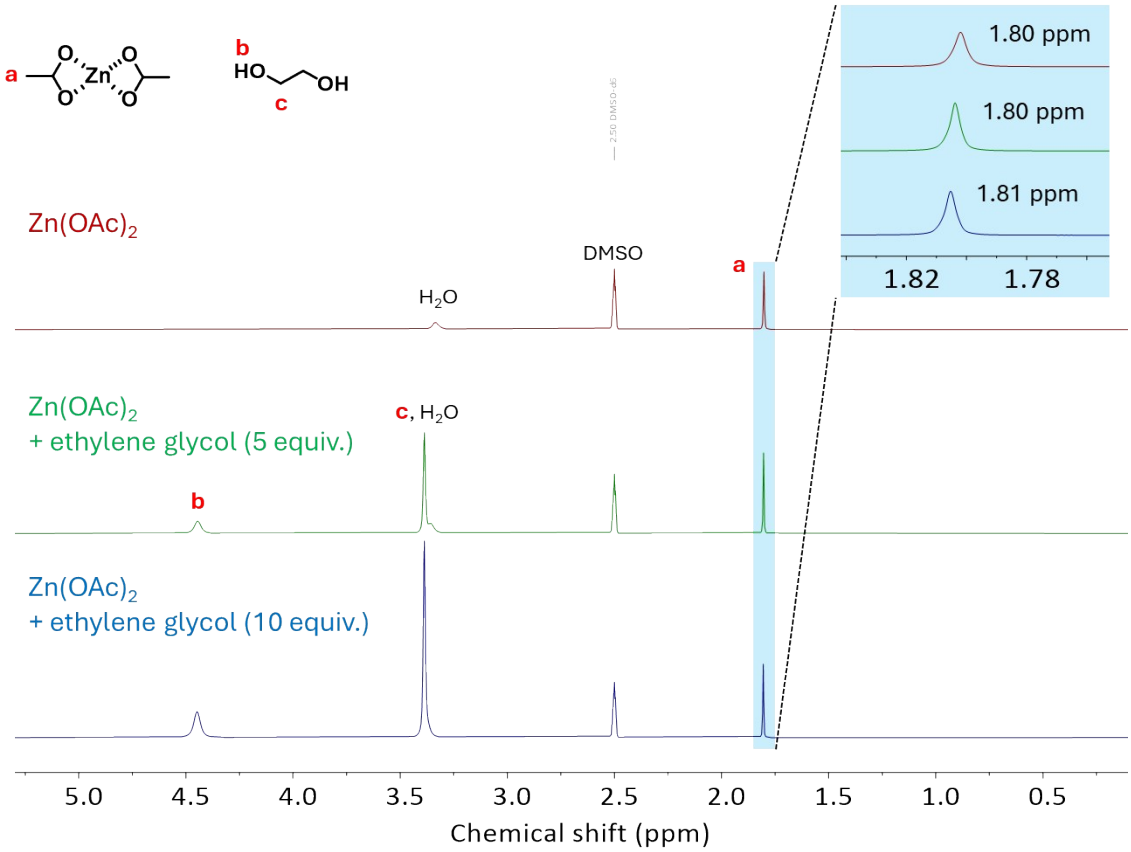

Fig. S13. Stacked ^{1}H NMR spectra of $Zn(OAc)_2$ and $Zn(OAc)_2$/ethylene glycol mixtures in DMSO-d_6 (298 K, 400 MHz).

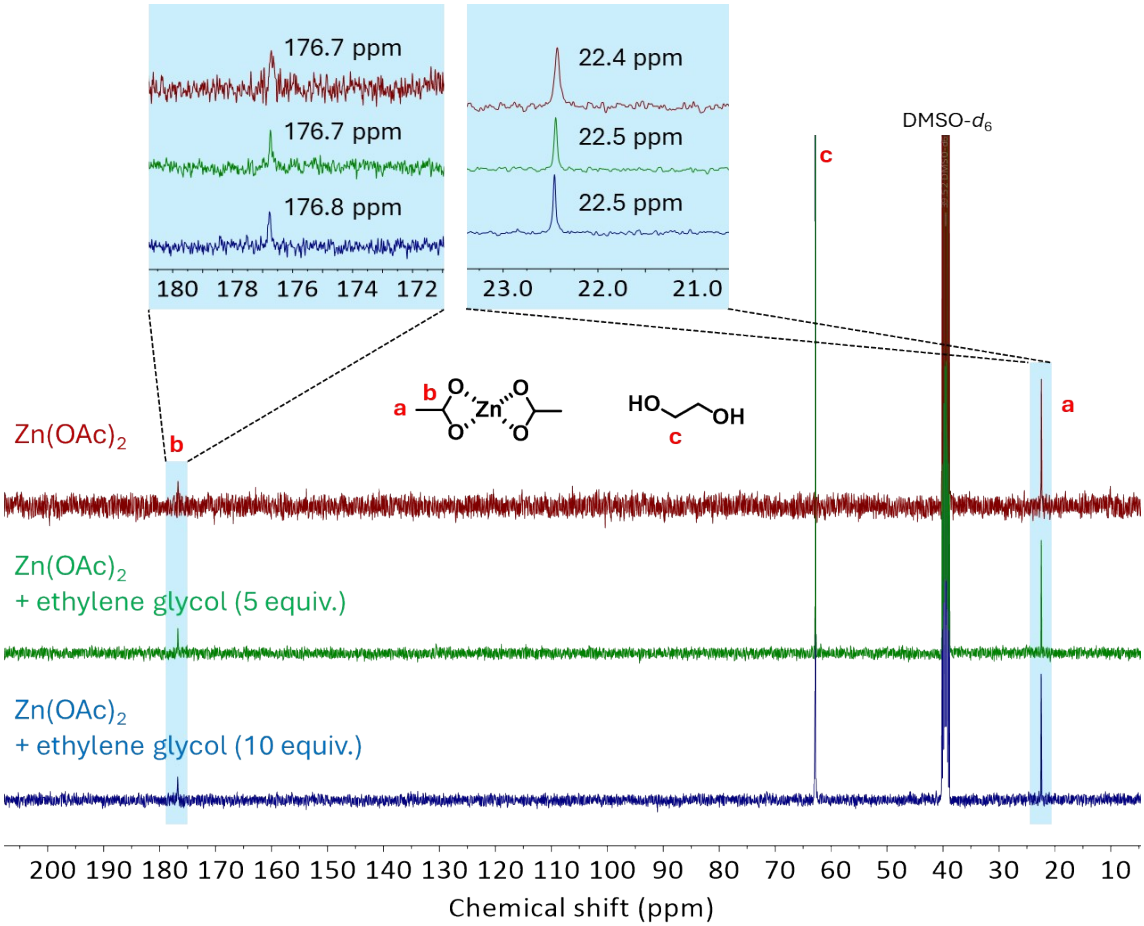

Fig. S14. Stacked ^{13}C NMR spectra of $Zn(OAc)_2$ and $Zn(OAc)_2$/ethylene glycol mixtures in DMSO-d_6 (298 K, 100 MHz).

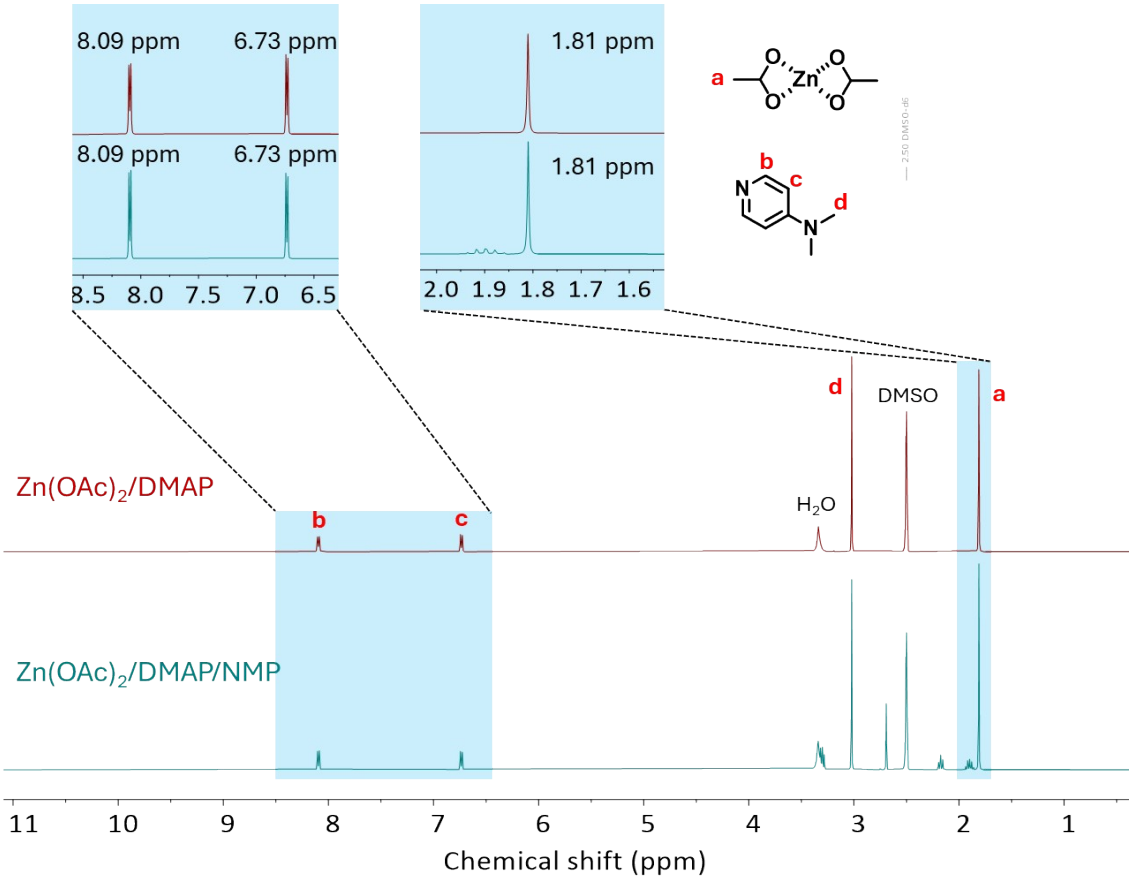

Fig. S15. Stacked ^{1}H NMR spectra of $Zn(OAc)_2$/DMAP and $Zn(OAc)_2$/DMAP/NMP mixtures in DMSO-d_6 (298 K, 400 MHz).

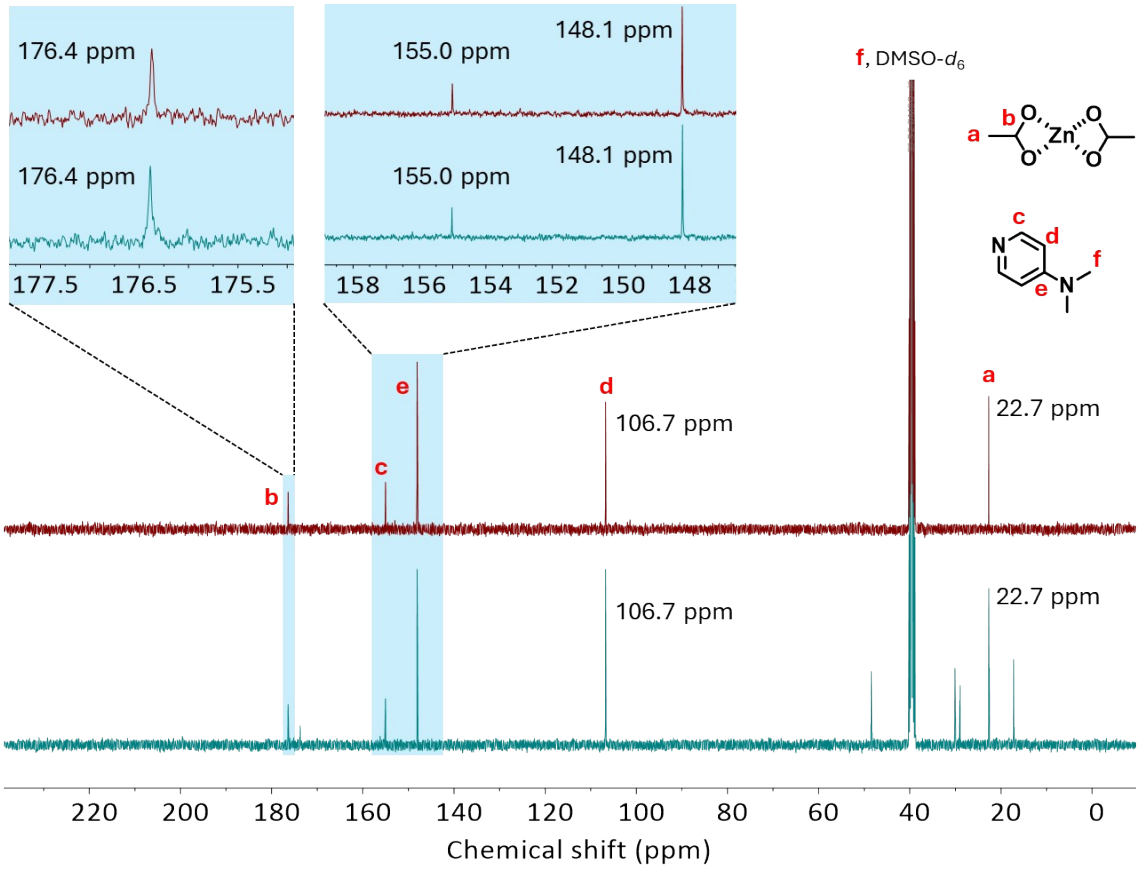

Fig. S16. Stacked ^{13}C NMR spectra of $Zn(OAc)_2$/DMAP and $Zn(OAc)_2$/DMAP/NMP mixtures in DMSO-d_6 (298 K, 400 MHz).

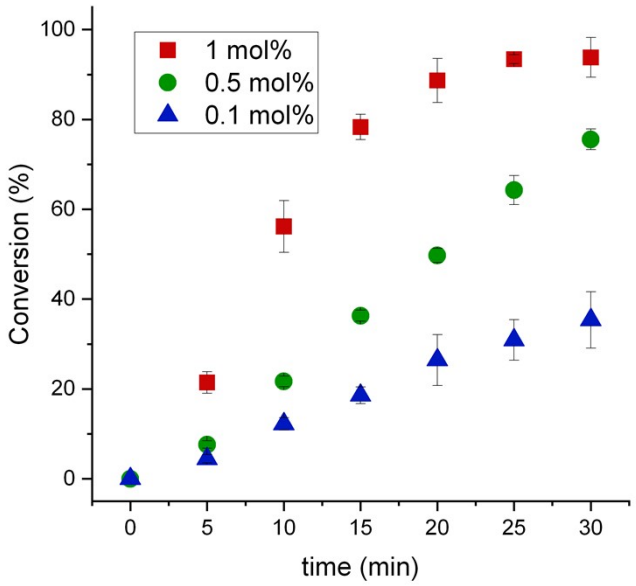

Fig. S17. Kinetic plots of PET conversions in glycolysis catalysed by $Zn(OAc)_2$/imidazole at different loading.

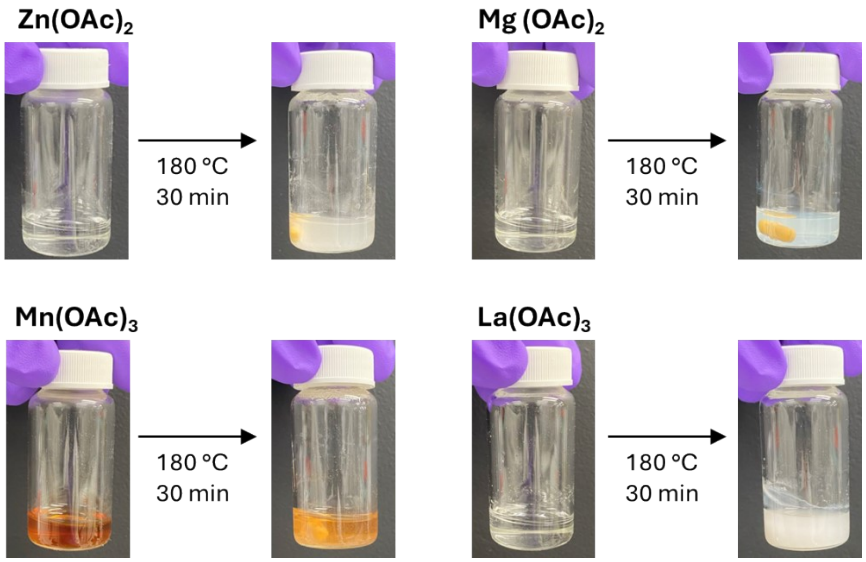

Fig. S18. Metal acetate solubility in ethylene glycol at 180 °C.

Computational Details

Initial modelling of the structures was carried out with GaussView 6.[3] The geometry of the modelled systems was optimised with the xTB[4] program package at the GFN2-xTB[5] level of theory. The other settings were set to default unless otherwise stated.

Conformational searches were performed on the xTB optimised structures with CREST[6, 7] at the GFN2-xTB[5] level of theory in gas phase. The energy window was set to 12 kcal·mol^{-1}. The other settings were set to default unless otherwise stated. Unless otherwise stated, the subsequent sorting of conformational ensembles was performed with the CREGEN procedure within CREST,[6, 7] with Cartesian root mean square deviation (RMSD) thresholds as determined for each system with the RMSD Trajectory Tool in VMD[8] using default configuration, except for hydrogen atoms, which were included in the RMSD calculations.

Due to high computational costs, the transition state and intermediate structures of PET glycolysis with $Zn(OAc)_2$/DMA and $Zn(OAc)_2$/ABCO were not optimised with xTB or conformationally searched. Instead, they were modelled starting from the structure of the lowest energy conformer of the $Zn(OAc)_2$/Im TS with Im replaced by DMA and ABCO, respectively. The transition state in the unbound pathway with $Zn(OAc)_2$/ABCO converged to a structure presenting two imaginary frequencies instead of one (the second corresponding to a methyl group rotation). Attempts were made to remove the second imaginary frequency, including manual displacement of this $-CH_3$ group, decreasing the maximum size for an optimisation step to 1, and with the analytical second derivatives calculated at every optimisation step (opt=(recalcfc=1,maxstep=1)). The resulting converged structure was either a TS still containing 2 imaginary frequencies or a minimum with no imaginary frequencies, hence the second lowest energy conformer with $Zn(OAc)_2$/Im was taken to model the transition state with $Zn(OAc)_2$/ABCO.

All density functional theory calculations were performed using the Gaussian 16, Revisions C.01[9] and C.02[10] quantum chemistry code. Geometry optimisations of the conformers were

carried out at the ωB97X-D/6-31G(d) level of theory.[11-15] Single point calculations were performed, unless otherwise stated, at the ωB97X-D/def2-TZVP level of theory.[11, 16, 17] The temperature set to 453 K and solvent effects were included using an implicit solvent method as implemented by the conductor-like polarisable continuum model[18, 19] (CPCM) with 1,2-ethanediol as the solvent, and the dielectric constant ε of the solvent set to 19.1[20] to account for the effect of the temperature in both the optimisations and single point energy calculations.

Quasi-harmonic Gibbs free energies using Cramer and Truhlar's quasi-harmonic treatment of entropy[21] and Head-Gordon's quasi-harmonic treatment of enthalpy[22] were extracted using the GoodVibes Python library[23] from the optimised structure files combined with the single point energy calculation files with the temperature set to 453.15 K and concentration values as given experimentally for each system. All other settings were left at default.

All structure visualisations were performed using GaussView 6[3], and structure images were generated with CYLview 1.0 beta.[24]

Full coordinates for all the stationary points, together with computed free Gibbs energy and vibrational frequency data, are available via the corresponding Gaussian 16 output files and GoodVibes files, stored in the digital repository: DOI:10.6084/m9.figshare.30751247 (private link for review purposes only: https://figshare.com/s/2f8f04a1a06be6f5b1d5).

General procedure for DFT modelling of non-metal systems

Low-energy conformations for the ground-state structures of the organobases (ABCO, DABCO, DMA, DMAP, Imidazole, and NMI), methyl benzoate, ethanol, ethyl benzoate, and methanol were searched with CREST[6, 7] with no constraints and an energy window of 12 kcal·mol^{-1}. The organobase DBU required optimisation with xTB[4] before performing conformational search with CREST.[6, 7] As the number of conformers obtained for each base was low (between 1 and 6 conformers), no ensemble sorting with CREGEN was performed.

DFT geometry optimisations of the resulting conformers and subsequent single point calculations along with quasi-harmonic Gibbs free energies computations were performed following the procedures described in the **Computational Details** section. The corresponding concentrations are indicated in **Tables S10**-**S12**.

DFT modelling of $Zn(OAc)_2$

$Zn(OAc)_2$ was optimised with xTB[4] before performing a conformational search with CREST. [6, 7] In both the xTB optimisation and conformational search, constraints were applied on the Zn1-O4 and Zn1-O5 bonds (**Fig.S19A**) to 2.0 Å. No ensemble sorting with CREGEN was performed. DFT geometry optimisations of the resulting conformers and subsequent single point calculations along with quasi-harmonic Gibbs free energies computations were performed following the procedures described in the **Computational Details** section. No ensemble sorting with CREGEN was performed for $Zn(OAc)_2$. The concentration is indicated in **Tables S10**-**S12**.

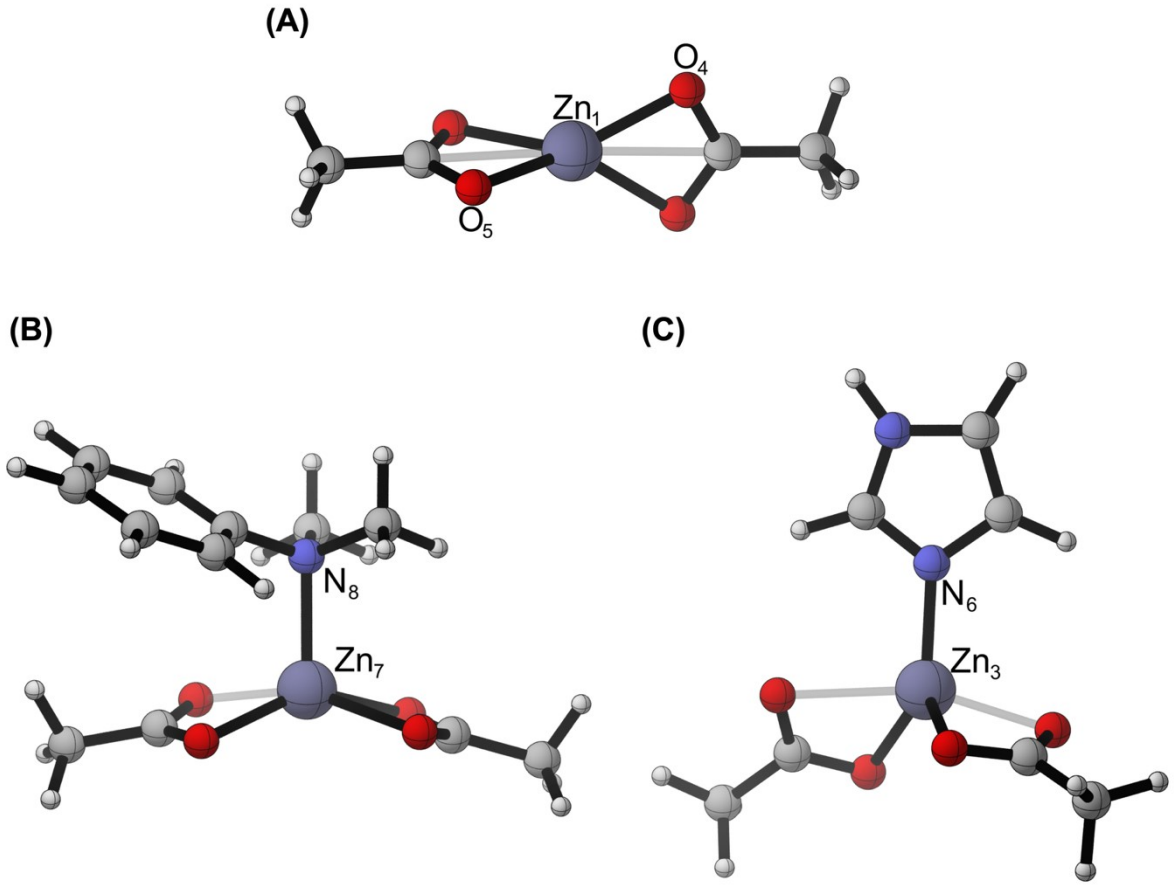

Fig.S19. Molecular geometries showing the numbering of the atoms and bonds constrained in the conformational search of: (A) $Zn(OAc)_2$; (B) $Zn(OAc)_2$/DMA; and (C) $Zn(OAc)_2$/Im

General procedure for DFT modelling of dual catalytic systems

$Zn(OAc)_2$/Base complexes were optimised with xTB[4] before performing a conformational search with CREST.[6, 7] In both the xTB optimisation and conformational search of $Zn(OAc)_2$/DMA, a constraint was applied on the Zn7-N8 (**Fig.19B**) bond at 2.0 Å. In the conformational search performed on $Zn(OAc)_2$/Im with CREST,[6, 7] a constraint was added to the Zn3-N6 (**Fig.S19C**) bond at 2.0 Å. Ensemble sorting with CREGEN was performed for $Zn(OAc)_2$/DMA and $Zn(OAc)_2$/DBU with RMSD thresholds of 0.786 Å and 0.836 Å, respectively. Redundant conformer elimination was not performed for $Zn(OAc)_2$/Im, $Zn(OAc)_2$/NMI, $Zn(OAc)_2$/DABCO, $Zn(OAc)_2$/DMAP, or $Zn(OAc)_2$/ABCO as the number of conformers generated by CREST for each of these systems was computationally affordable (between 7 and 18 conformers).

DFT geometry optimisations of the resulting conformers and subsequent single point calculations along with quasi-harmonic Gibbs free energies computations were performed following the procedures described in the **Computational Details** section. The corresponding concentrations are indicated in **Tables S10**-**S12**.

Binding of the dual catalytic complexes

Table S10 shows the quasi-harmonic Gibbs free energies (qhG) obtained with Cramer and Truhlar's vibrational entropy approach and Head-Gordon's quasi-harmonic approximation in enthalpy calculations for the lowest energy conformers of the Lewis acid, bases, and dual catalysts.

Binding free energies ($^{\Delta G_{binding}}$, **Table S10**) of $Zn(OAc)_2$/base complexes were computed using **Equation S2**, where $qhG(Zn(OAc)_2/base)$ is the quasi-harmonic Gibbs free energy of the dual catalyst; $qhG(Zn(OAc)_2)$ is the quasi-harmonic Gibbs free energy of the Lewis acid, and $qhG(base)$ is the quasi-harmonic Gibbs free energy of the base.

$$\Delta G_{binding} = qhG(Zn(OAc)_2/base) - \left(qhG\left(Zn(OAc)_2\right) + qhG(base)\right) \quad (2)$$

Table S10. Computed quasi-harmonic Gibbs free energies at 453.15 K and 0.0089 mol·L^{-1} using the thermal corrections obtained in the optimisations at the ωB97X-D/6-31G(d) level of theory[11-15] combined with the single point calculation electronic energies at the ωB97X-D/def2-TZVP level of theory,[11, 16, 17] with both including the CPCM implicit solvent model for 1,2-ethanediol at 453 K (ε = 19.1), for the catalytic systems, with Cramer and Truhlar's vibrational entropy approach and Head-Gordon's quasi-harmonic approximation in enthalpy calculations.

	Structure	**qhG_{spc} (E_h)**	**$\Delta G_{binding}$ (kcal·mol^{-1})**
Lewis acid	$Zn(OAc)_2$	-2236.538249	
Bases	DMA	-366.111211	
	Im	-226.209427	
	NMI	-265.496439	
	DABCO	-345.222543	
	DMAP	-382.170018	
	ABCO	-329.190133	
	DBU	-461.942314	
Dual catalysts	$Zn(OAc)_2$/DMA	-2602.632253	10.797547
	$Zn(OAc)_2$/Im	-2462.748052	-0.235943
	$Zn(OAc)_2$/NMI	-2502.035318	-0.395331
	$Zn(OAc)_2$/DABCO	-2581.759945	0.531500
	$Zn(OAc)_2$/DMAP	-2618.708676	-0.256651
	$Zn(OAc)_2$/ABCO	-2565.728187	0.122364

	$Zn(OAc)_2$/DBU	-2698.487414	-4.299064

Natural Bond Orbital analysis

The Natural Bond Orbital (NBO) analysis was performed on the dual catalytic complexes. The subsequent natural charges on the zinc ion and the nitrogen were plotted for each combination of $Zn(OAc)_2$/Base catalyst (**Fig. S20a** and **b**). Pearson's correlation coefficients (r) were computed to measure the linear correlation between the natural charge and Gibbs free binding energies. The obtained correlations were r = 0.56 in the case of the natural charge of zinc ion and the Gibbs free binding energies of the dual catalysts, and r = 0.71 in the case of the natural charge of nitrogen and the Gibbs free binding energies of the dual catalysts. Although these values suggest a moderate correlation between the natural charges and the Gibbs free binding energies of the dual catalysts, it is difficult to estimate the degree of bias in such a small dataset.

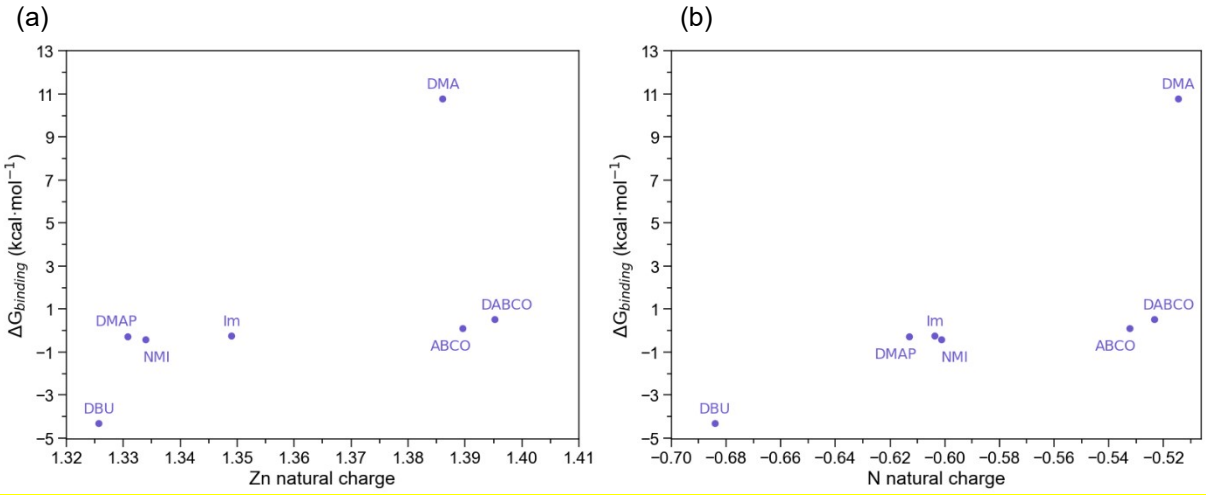

Figure S20. Gibbs free binding energies of the dual catalysts as a function of: (a) natural charge of zinc ion and (b) natural charge of nitrogen.

The same analysis was performed on the Mulliken charges (**Fig. S21a** and **b**). In this case, the correlation between the Mulliken charge of the zinc ion and the Gibbs free energies was 0.89, whereas the correlation between the Mulliken charge of the nitrogen atom and the Gibbs free energies was 0.19. Here, it is suggested that the Mulliken charge of the nitrogen and the Gibbs free energies are not correlated, whereas the correlation is high between the Mulliken charge of the zinc ion and the Gibbs free energies. Similarly to the natural charges, the results may be subject to bias that cannot be captured in such small sample.

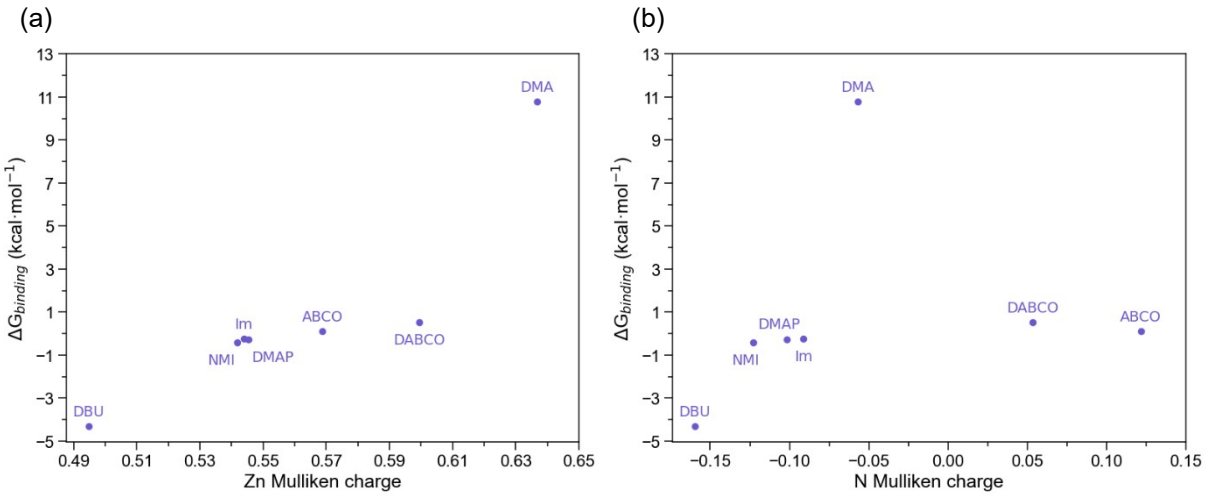

Figure S21. Gibbs free binding energies of the dual catalysts as a function of: (a) Mulliken charge of zinc ion and (b) Mulliken charge of nitrogen

DFT Modelling of PET glycolysis: transition states

The transition state structure of the bound pathway promoted by $Zn(OAc)_2$/Im ($TS_{III\text{-}IVa}$, **Table S10**) was optimised with xTB[4] prior to the conformational search with CREST[6, 7] constraining the C7-O21 and O21-H50 bonds (**Fig.S22A**) to 1.6 Å and 1.2 Å, respectively, in both cases. Redundant conformer elimination was performed with the ensemble sorting algorithm CREGEN on the conformers with an RMSD of 0.548 Å.

The structure for the transition state in the unbound pathway promoted by $Zn(OAc)_2$/Im ($TS_{III\text{-}IVb}$, **Table S11**) was also first optimised with xTB[4] constraining the C7-O21 and O20-H50 bonds (**Fig.S22B**) to 1.6 Å and 1.2 Å, respectively. These constraints were also used in the conformational search with CREST. The sorting of conformational ensembles was performed with the CREGEN procedure with an RMSD of 0.684 Å.

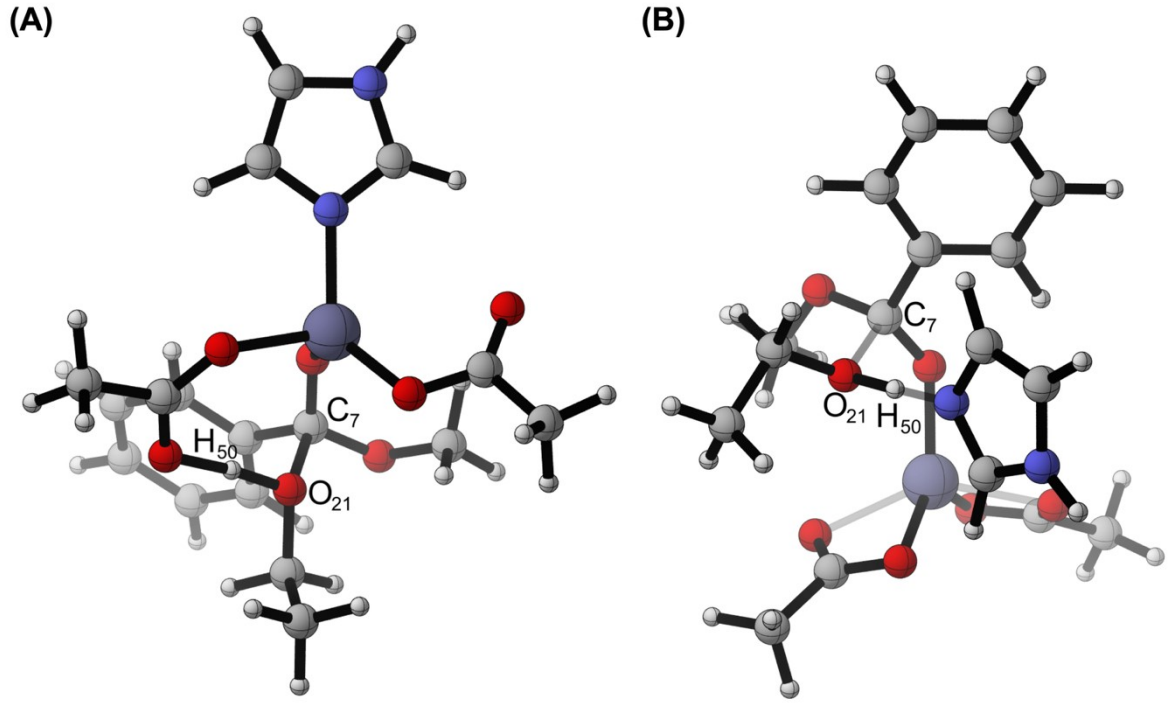

Fig.S22. Molecular geometries showing the numbering of the atoms and bonds constrained in the conformational search of: (A) the transition state in the bound pathway promoted by $Zn(OAc)_2$/Im ($TS_{III\text{-}IVa}$); and (B) the transition state in the unbound pathway promoted by $Zn(OAc)_2$/Im ($TS_{III\text{-}IVb}$)

Due to the large number of conformers obtained after ensemble sorting of both transition states (195 for the TS in the bound pathway and 157 for the TS in the unbound pathway), single point calculations at the ωB97X-D/6-31G(d)[11-15] level of theory using the CPCM implicit solvent model for 1,2-ethanediol at the temperature of 453 K (ε = 19.1) were performed on each of them. All the conformers of the bound and unbound transition states within 3 kcal·mol^{-1} and 2 kcal·mol^{-1} from the respective lowest energy conformer to make the number of conformers manageable were optimised with DFT following the procedure detailed in the **Computational Details** section, with the subsequent single point calculations along with quasi-harmonic Gibbs free energies computations.

Transition state structures of PET glycolysis with $Zn(OAc)_2$/DMA in both pathways ($TS_{III\text{-}IVc}$ and $TS_{III\text{-}IVd}$, **Table S12**) were modelled starting from the structure of the lowest energy conformer of the $Zn(OAc)_2$/Im TS with Im replaced by DMA. These were not optimised with xTB or conformationally searched. Instead, they were optimised with DFT following the procedure detailed in the **Computational Details** section, with the subsequent single point calculations along with quasi-harmonic Gibbs free energies computations.

The same procedure was followed for the transition state structures of PET glycolysis with $Zn(OAc)_2$/ABCO ($TS_{III\text{-}IVe}$ and $TS_{III\text{-}IVf}$, **Table S13**). These were modelled starting from the structure of the lowest energy conformer of the $Zn(OAc)_2$/Im TS with Im replaced by ABCO. In the case of the unbound pathway, the conformer converged to a structure presenting two imaginary frequencies, with the second one corresponding to the rotation of a methyl group. For this reason, the second lowest energy conformer of the transition state with $Zn(OAc)_2$/Im ($\Delta G_{(lowest\ -\ second\ lowest)}$ = 0.1 kcal·mol^{-1}) was taken to model the transition state with $Zn(OAc)_2$/ABCO.

Similarly, the transition state structure of PET glycolysis with $Zn(OAc)_2$ ($TS_{III\text{-}IVg}$, **Table S14**) only was modelled starting from the lowest energy conformer of $Zn(OAc)_2$/Im TS in the bound pathway, where Im was removed from the system. This was not optimised with xTB or conformationally searched. Instead, it was optimised with DFT following the procedure

detailed in the **Computational Details** section, with the subsequent single point calculation along with quasi-harmonic Gibbs free energies computation.

The transition state structure of PET glycolysis with imidazole only ($TS_{III\text{-}IVh}$, **Table S15**), was modelled starting from the lowest energy conformer of $Zn(OAc)_2$/Im TS in the unbound pathway, where $Zn(OAc)_2$ was removed from the system. This was not optimised with xTB or conformationally searched. Instead, it was optimised with DFT following the procedure detailed in the **Computational Details** section, with the subsequent single point calculation along with quasi-harmonic Gibbs free energies computation. This same procedure was followed for the transition state structure of PET glycolysis with DMA ($TS_{III\text{-}IVi}$, **Table S16**) and ABCO ($TS_{III\text{-}IVj}$, **Table S17**) only, where the structures were respectively modelled in this case from the optimised $Zn(OAc)_2$/DMA TS and $Zn(OAc)_2$/ABCO TS in the unbound pathway.

Fig.S26 contains a summary of computed Gibbs free energy barriers of PET glycolysis associated with the use of single components and dual catalysts.

DFT Modelling of PET glycolysis: intermediate systems

Both structures were optimised with xTB[4] with no constraints and conformational searches with CREST[6, 7] were subsequently performed. RMSD values of 1.319 Å and 0.533 Å were respectively used as the thresholds in the redundant conformer eliminations of Intermediates III_c and IV_c with CREGEN. Due to the large number of conformers obtained after ensemble sorting of both intermediate structures (94 and 114, respectively, for intermediates III_a and IV_a), single point calculations at the ωB97X-D/6-31G(d) level of theory[11-15] with the CPCM implicit solvent model for 1,2-ethanediol at 453 K (ε = 19.1) were performed on each of them. To make the number of conformers manageable, only the conformers of the intermediate III_a within 2.5 kcal·mol^{-1} from the lowest energy conformer and the conformers of the intermediate IV_a within 2 kcal·mol^{-1} from the lowest energy conformer were optimised following the procedure detailed in the **Computational Details** section, with the subsequent single point calculations along with quasi-harmonic Gibbs free energies computations.

The π-π stacking in the intermediate III_a is shown in **Fig.S23** together with atom distances between the phenyl ring and imidazole.

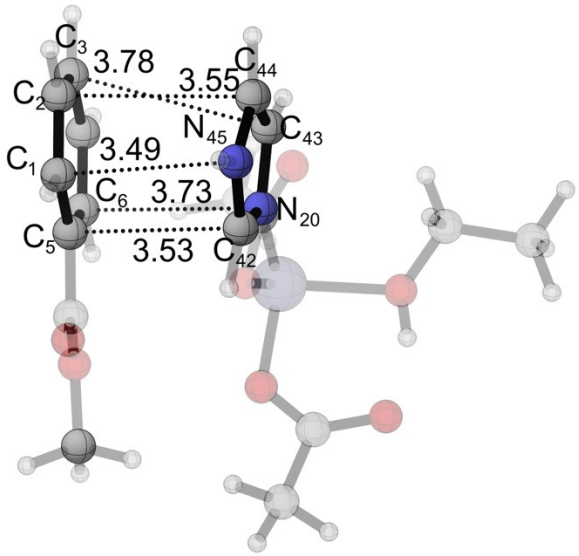

Fig.S23. Molecular geometries showing the numbering of the atoms and π-π stacking distances of Intermediate III_a

Energy profiles of PET glycolysis

Free energies (ΔG, **Table S11**, **Table S12**, and **Table S13**) were computed using **Equation S3**, where $qhG(structure)$ is the quasi-harmonic Gibbs free energy of the system of each step, and $qhG(reference)$ is the sum of quasi-harmonic Gibbs free energies of the starting materials.

$$\Delta G = qhG(structure) - qhG(reference) \quad (3)$$

The reaction profiles of the glycolysis of PET promoted by $Zn(OAc)_2$/DMA and $Zn(OAc)_2$/ABCO were also represented and these can be found in **Figures S24** and **S25**, respectively.

Table S11. Computed quasi-harmonic Gibbs free energies at 453.15 K and concentration indicated using the thermal corrections obtained in the optimisations at the ωB97X-D/6-31G(d) level of theory[11-

[15] combined with the single point calculation electronic energies at the ωB97X-D/def2-TZVP level of theory[11, 16, 17] with both including the CPCM implicit solvent model for 1,2-ethanediol at 453 K (ε = 19.1), and computed free energies of PET glycolysis catalysed by $Zn(OAc)_2$/Im in the bound and unbound pathways

	Structures	**Conc. (mol/L)**	**qh G (E_h)**	**ΔG (kcal·mol^{-1})**
Starting materials	$Zn(OAc)_2$	0.0089	-2236.538249	–
	Im	0.0089	-226.209427	–
	EtOH	17.857	-155.012927	–
	Methyl benzoate (PET model)	0.893	-460.061833	–
	$Zn(OAc)_2$ + Im + EtOH + PET	–	-3077.822436	0.0 (reference)
	$Zn(OAc)_2$/Im + EtOH + PET	0.0089	-2462.748052	-0.235943
Bound pathway. Imidazole acts as a ligand to the zinc acetate	III_a	0.0089	-3077.807350	9.466601
	$TS_{III\text{-}IVa}$	0.0089	-3077.768486	33.854111
	IV_a	0.0089	-3077.776617	28.751835
Unbound pathway.	$TS_{III\text{-}IVb}$	0.0089	-3077.755903	41.750056

Imidazole acts as a base, independent of the zinc acetate				
	Ethyl benzoate + MeOH + $Zn(OAc)_2$/Im	0.0089	-3077.840195	-11.143932
Final products	Ethyl benzoate + MeOH + $Zn(OAc)_2$ + Im	0.0089	-3077.839819	-10.907989

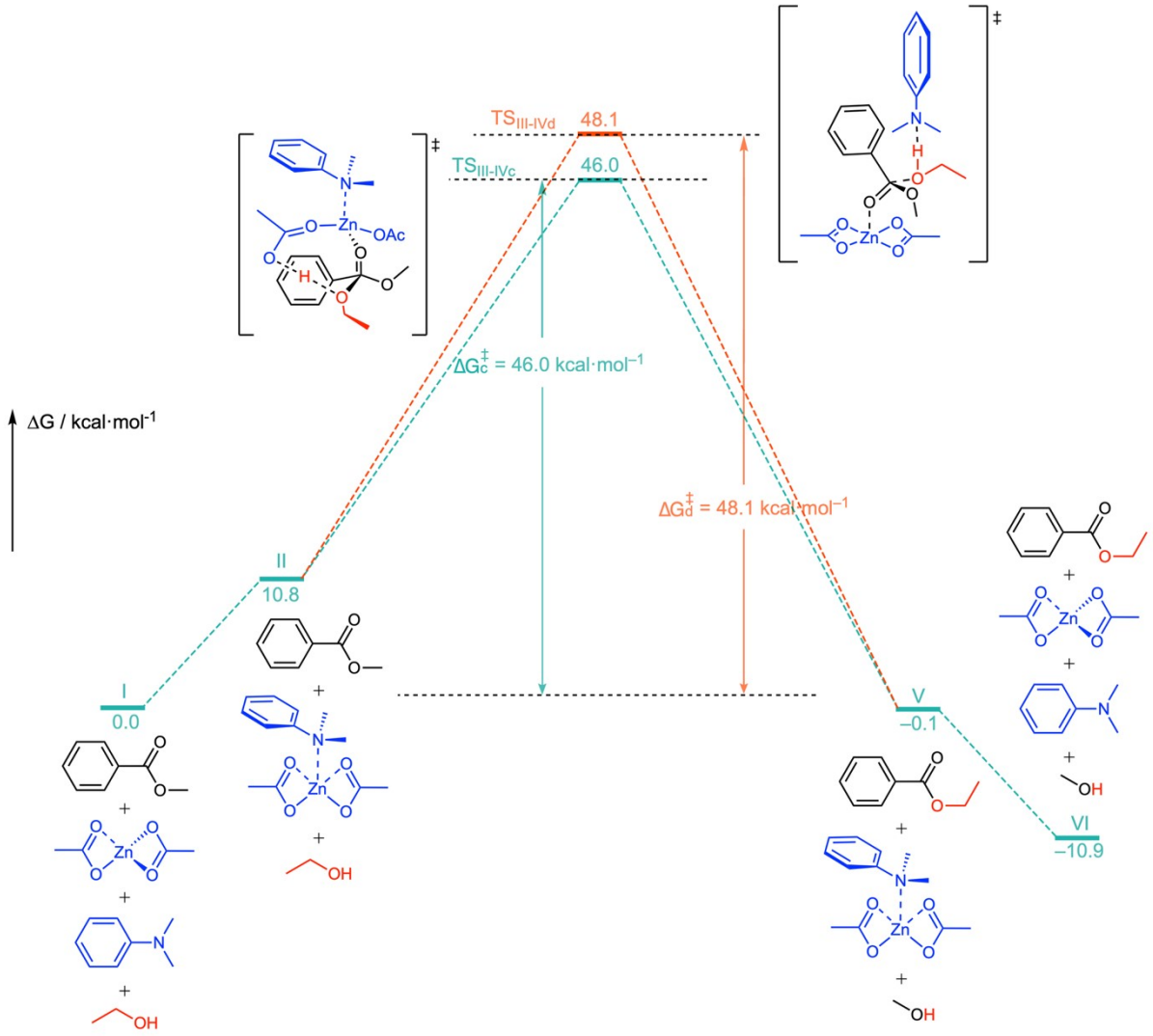

Fig.S24. PET glycolysis catalysed by $Zn(OAc)_2$/DMA in the bound (green) and unbound (orange) pathways: calculated Gibbs free energy profile at 453.15 K. The structures were optimised at ωB97X-D/6-31G(d) level of theory and with single point energy calculation at the ωB97X-D/def2-TZVP level of theory, with both including the CPCM implicit solvent model for 1,2-ethanediol at 453 K (ε = 19.1)

Table S12. Computed quasi-harmonic Gibbs free energies at 453.15 K and concentration indicated using the thermal corrections obtained in the optimisations at the ωB97X-D/6-31G(d) level of theory[11-15] combined with the single point calculation electronic energies at the ωB97X-D/def2-TZVP level of theory,[11, 16, 17] with both including the CPCM implicit solvent model for 1,2-ethanediol at 453 K (ε = 19.1), and computed free energies of PET glycolysis catalysed by $Zn(OAc)_2$/DMA in the bound and unbound pathways

	Structures	**Conc. (mol/L)**	**qh G (E_h)**	**ΔG (kcal·mol^{-1})**
Starting materials	$Zn(OAc)_2$	0.0089	-2236.538249	–
	DMA	0.0089	-366.111211	–
	EtOH	17.857	-155.012927	–
	Methyl benzoate (PET model)	0.893	-460.061833	–
	$Zn(OAc)_2$ + DMA + EtOH + PET	–	-3217.724220	0.0 (reference)
	$Zn(OAc)_2$/DMA + EtOH + PET	0.0089	-2602.632253	10.797547
Bound pathway. DMA acts as a ligand to the zinc acetate	$TS_{III\text{-}IVc}$	0.0089	-3217.650873	46.025903

Unbound pathway. DMA acts as a base, independent of the zinc acetate	$TS_{III-IVd}$	0.0089	-3217.647571	48.097937
	Ethyl benzoate + MeOH + $Zn(OAc)_2$/DMA	0.0089	-3217.724396	-0.110442
Final products	Ethyl benzoate + MeOH + $Zn(OAc)_2$ + DMA	0.0089	-3217.741603	-10.907989

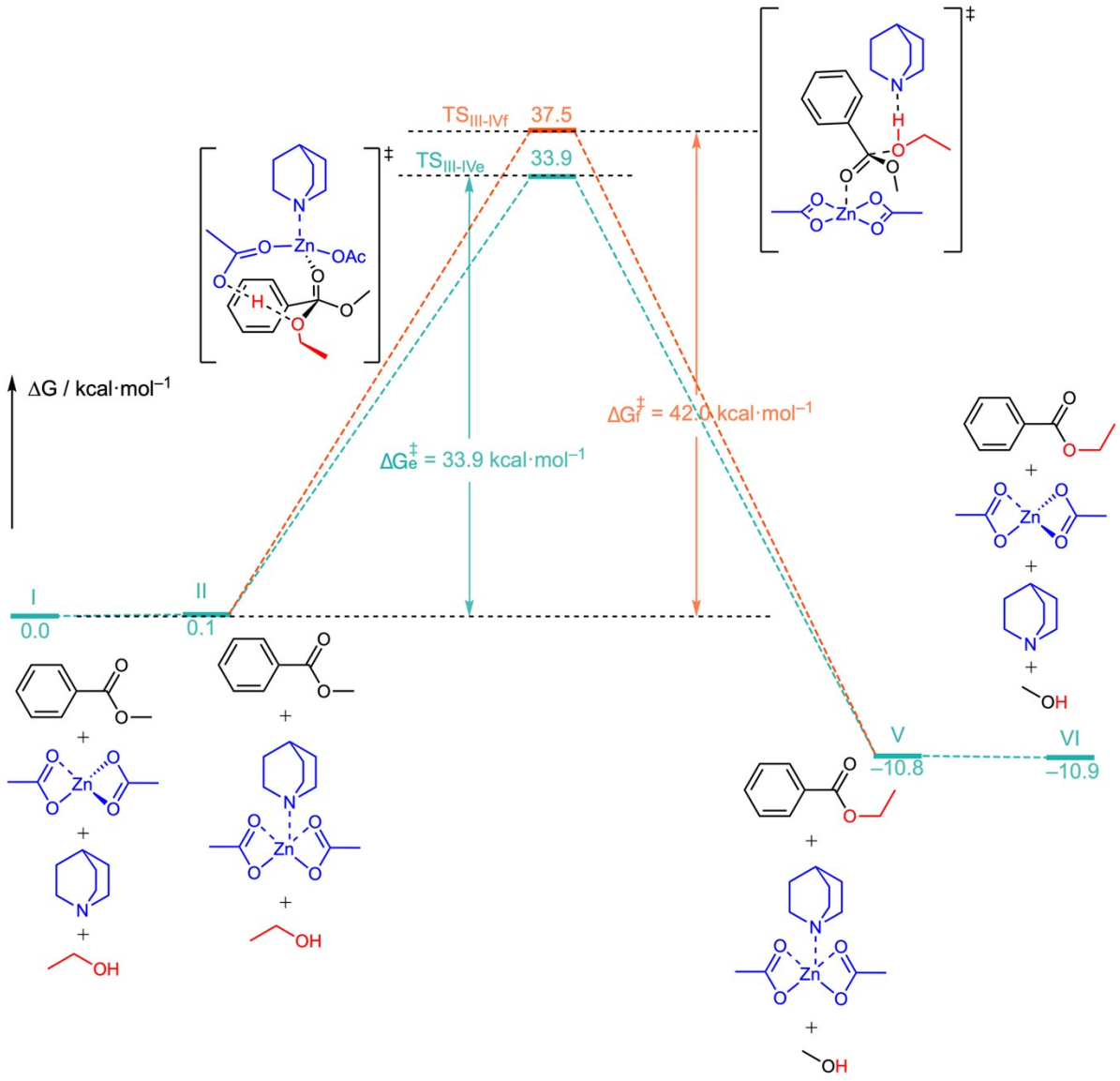

Fig.S25. PET glycolysis catalysed by $Zn(OAc)_2$/ABCO in the bound (green) and unbound (orange) pathways: calculated Gibbs free energy profile at 453.15 K. The structures were optimised at ωB97X-D/6-31G(d) level of theory and with single point energy calculation at the ωB97X-D/def2-TZVP level of theory, with both including the CPCM implicit solvent model for 1,2-ethanediol at 453 K (ε = 19.1).

Table S13. Computed quasi-harmonic Gibbs free energies at 453.15 K and concentration indicated using the thermal corrections obtained in the optimisations at the ωB97X-D/6-31G(d) level of theory[11-15] combined with the single point calculation electronic energies at the ωB97X-D/def2-TZVP level of theory,[11, 16, 17] with both including the CPCM implicit solvent model for 1,2-ethanediol at 453 K (ε = 19.1), and computed free energies of PET glycolysis catalysed by $Zn(OAc)_2$/ABCO in the bound and unbound pathways

	Structures	**Conc. (mol/L)**	**qh G (E_h)**	**ΔG (kcal·mol^{-1})**
Starting materials	$Zn(OAc)_2$	0.0089	-2236.538249	–
	ABCO	0.0089	-329.190133	–
	EtOH	17.857	-155.012927	–
	Methyl benzoate (PET model)	0.893	-460.061833	–
	$Zn(OAc)_2$ + ABCO + EtOH + PET	–	-3180.803142	0.0 (reference)
	$Zn(OAc)_2$/ABCO + EtOH + PET	0.0089	-2565.728187	0.122364
Bound pathway. ABCO acts as a ligand to the zinc acetate	$TS_{III\text{-}IVe}$	0.0089	-3180.749123	33.897409

Unbound pathway. ABCO acts as a base, independent of the zinc acetate	$TS_{III-IVf}$	0.0089	-3180.743390	37.494918
	Ethyl benzoate + MeOH + $Zn(OAc)_2$/ABCO	0.0089	-3180.820330	-10.785625
Final products	Ethyl benzoate + MeOH + $Zn(OAc)_2$ + ABCO	0.0089	-3180.820525	-10.907989

As shown in the graph below (**Fig.S26**) and **Tables S14–S17** containing the computed free energies, the use of a single component presents a higher Gibbs free energy barrier than the dual catalytic systems $Zn(OAc)_2$/Im and $Zn(OAc)_2$/ABCO, emphasising the cooperativity of these catalysts. The exception in this case was $Zn(OAc)_2$/DMA, in which the barrier is 11.3 kcal/mol higher than when only $Zn(OAc)_2$ is used, suggesting this dual catalyst may follow a different mechanism as discussed in the main text.

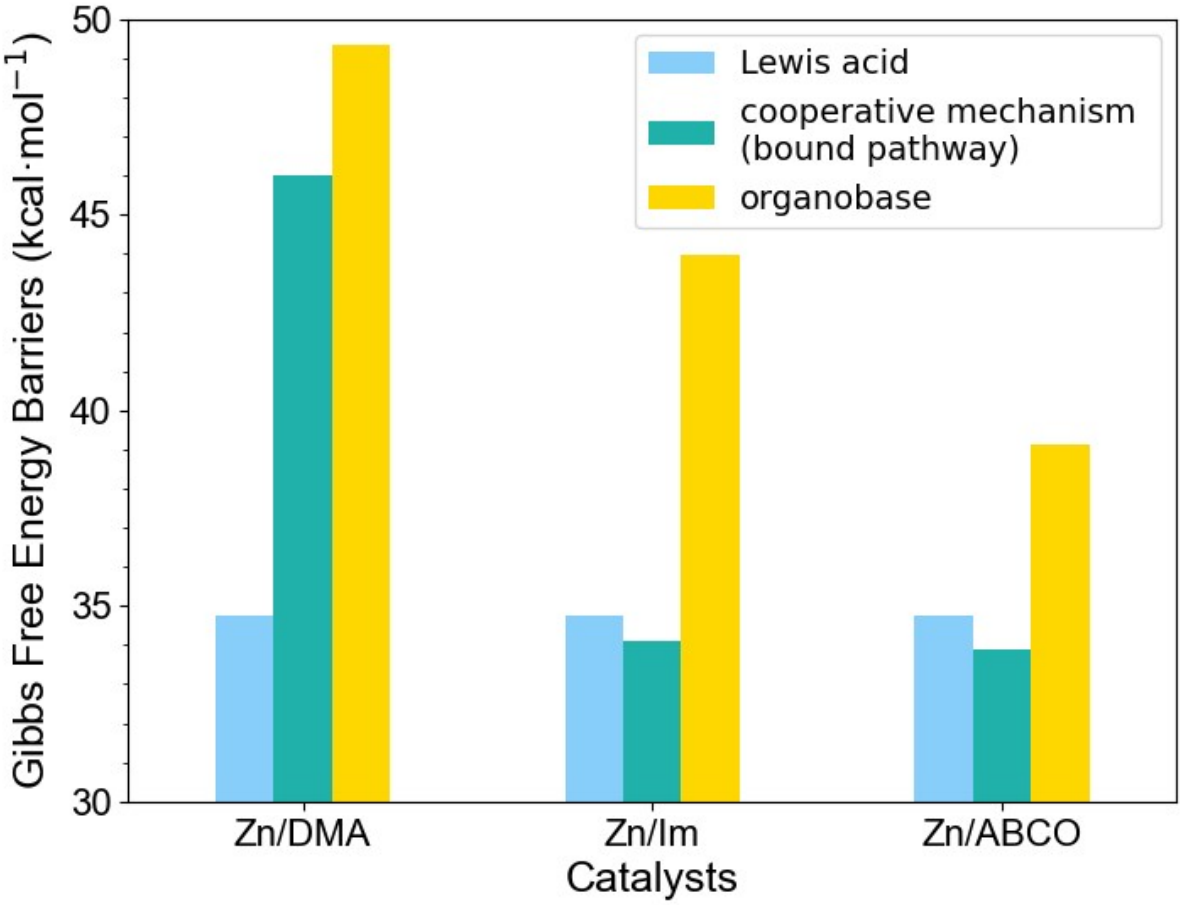

Fig.S26. Gibbs free energy barriers for Zn(OAc)2, Zn(OAc)2/base, and base systems (base = DMA, Im, ABCO). The systems were optimised at ωB97X-D/6-31G(d) level of theory and with single point energy calculation at the ωB97X-D/def2-TZVP level of theory, both with the CPCM implicit solvent model for 1,2-ethanediol at 453 K (ε = 19.1).

Table S14. Computed quasi-harmonic Gibbs free energies at 453.15 K and concentration indicated using the thermal corrections obtained in the optimisations at the ωB97X-D/6-31G(d) level of theory[11-15] combined with the single point calculation electronic energies at the ωB97X-D/def2-TZVP level of theory[11, 16, 17] with both including the CPCM implicit solvent model for 1,2-ethanediol at 453 K (ε = 19.1), and computed free energies of PET glycolysis catalysed by $Zn(OAc)_2$

	Structures	Conc. (mol/L)	qh G (E_h)	ΔG (kcal·mol^{-1})
Starting materials	$Zn(OAc)_2$	0.0089	-2236.538249	–
	EtOH	17.857	-155.012927	–
	Methyl benzoate (PET model)	0.893	-460.061833	–
	$Zn(OAc)_2$ + EtOH + PET	–	-2851.613009	0.0 (reference)
Lewis acid pathway. $Zn(OAc)_2$ is the only catalyst	$TS_{III\text{-}IVg}$	0.0089	-2851.557642	34.743291
Final products	Ethyl benzoate + MeOH + $Zn(OAc)_2$	0.0089	-2851.630392	-10.907989

Table S15. Computed quasi-harmonic Gibbs free energies at 453.15 K and concentration indicated using the thermal corrections obtained in the optimisations at the ωB97X-D/6-31G(d) level of theory[11-15] combined with the single point calculation electronic energies at the ωB97X-D/def2-TZVP level of theory[11, 16, 17] with both including the CPCM implicit solvent model for 1,2-ethanediol at 453 K (ε = 19.1), and computed free energies of PET glycolysis catalysed by Im

	Structures	Conc. (mol/L)	qh G (E_h)	ΔG (kcal·mol^{-1})
Starting	Im	0.0089	-226.209427	–

materials	EtOH	17.857	-155.012927	–
	Methyl benzoate (PET model)	0.893	-460.061833	–
	Im + EtOH + PET	–	-841.284187	0.0 (reference)
Organic base pathway. Im is the only catalyst	$TS_{III\text{-}IVh}$	0.0089	-841.214123	43.965791
Final products	Ethyl benzoate + MeOH + Im	0.0089	-841.301570	-10.907989

Table S16. Computed quasi-harmonic Gibbs free energies at 453.15 K and concentration indicated using the thermal corrections obtained in the optimisations at the ωB97X-D/6-31G(d) level of theory[11-15] combined with the single point calculation electronic energies at the ωB97X-D/def2-TZVP level of theory[11, 16, 17] with both including the CPCM implicit solvent model for 1,2-ethanediol at 453 K (ε = 19.1), and computed free energies of PET glycolysis catalysed by DMA

	Structures	**Conc. (mol/L)**	**qh G (E_h)**	**ΔG (kcal·mol^{-1})**
Starting materials	DMA	0.0089	-366.111211	–
	EtOH	17.857	-155.012927	–
	Methyl benzoate (PET model)	0.893	-460.061833	–
	DMA + EtOH +	–	-981.185971	0.0 (reference)

	PET			
Organic base pathway. DMA is the only catalyst	$TS_{III-IVi}$	0.0089	-981.107334	49.345425
Final products	Ethyl benzoate + MeOH + DMA	0.0089	-981.203354	-10.907989

Table S17. Computed quasi-harmonic Gibbs free energies at 453.15 K and concentration indicated using the thermal corrections obtained in the optimisations at the ωB97X-D/6-31G(d) level of theory[11-15] combined with the single point calculation electronic energies at the ωB97X-D/def2-TZVP level of theory[11, 16, 17] with both including the CPCM implicit solvent model for 1,2-ethanediol at 453 K (ε = 19.1), and computed free energies of PET glycolysis catalysed by ABCO

	Structures	**Conc. (mol/L)**	**qh G (E_h)**	**ΔG (kcal·mol^{-1})**
Starting materials	ABCO	0.0089	-329.190133	–
	EtOH	17.857	-155.012927	–
	Methyl benzoate (PET model)	0.893	-460.061833	–
	ABCO + EtOH + PET	–	-944.264893	0.0 (reference)
Organic base pathway. ABCO is the	$TS_{III-IVj}$	0.0089	-944.202549	39.121421

only catalyst				
Final products	Ethyl benzoate + MeOH + ABCO	0.0089	-944.282276	-10.907989

Table S18. Computed quasi-harmonic Gibbs free energies at 453.15 K and concentration indicated using the thermal corrections obtained in the optimisations at the ωB97X-D/6-31G(d) level of theory[11-15] combined with the single point calculation electronic energies at the ωB97X-D/def2-TZVP level of theory,[11, 16, 17] with both including the CPCM implicit solvent model for 1,2-ethanediol at 453 K (ε = 19.1), and computed free energies of PET glycolysis catalysed by $Zn(OAc)_2$/DBU in the bound and unbound pathways

	Structures	**Conc. (mol/L)**	**qh G (E_h)**	**ΔG (kcal·mol^{-1})**
Starting materials	$Zn(OAc)_2$	0.0089	-2236.538249	–
	DBU	0.0089	-461.942314	–
	EtOH	17.857	-155.012927	–
	Methyl benzoate (PET model)	0.893	-460.061833	–
	$Zn(OAc)_2$ + DBU + EtOH + PET	–	-3313.555323	0.0 (reference)
	$Zn(OAc)_2$/DBU + EtOH + PET	0.0089	-3313.562174	-4.299064
Bound pathway. DBU acts as a ligand to the zinc acetate	$TS_{III-IVk}$	0.0089	-3313.503780	36.642761
Unbound pathway. DBU acts as a base, independent of the zinc acetate	$TS_{III-IVl}$	0.0089	-3313.501000	38.387236
	Ethyl benzoate + MeOH + $Zn(OAc)_2$/DBU	0.0089	-3313.579557	-15.207053

Final products	Ethyl benzoate + MeOH + $Zn(OAc)_2$ + DBU	0.0089	-3313.572706	-10.907989

References

1. C. Jehanno, J. Demarteau, D. Mantione, M. C. Arno, F. Ruipérez, J. L. Hedrick, A. P. Dove and H. Sardon, *Angew. Chem. Int. Ed.*, 2021, **60**, 6710-6717.
2. B. Liu, W. Fu, X. Lu, Q. Zhou and S. Zhang, *ACS Sustain. Chem. Eng.*, 2018, **7**, 3292-3300.
3. R. Dennington, T. A. Keith and J. M. Millam, *GaussView, Version 6*, Semichem Inc., Shawnee Mission, KS, 2016.
4. C. Bannwarth, E. Caldeweyher, S. Ehlert, A. Hansen, P. Pracht, J. Seibert, S. Spicher and S. Grimme, *Wiley Interdiscip. Rev. Comput. Mol. Sci.*, 2021, **11**, e1493.
5. C. Bannwarth, S. Ehlert and S. Grimme, *J. Chem. Theory Comput.*, 2019, **15**, 1652-1671.
6. S. Grimme, *J. Chem. Theory Comput.*, 2019, **15**, 2847-2862.
7. P. Pracht, F. Bohle and S. Grimme, *Phys. Chem. Chem. Phys.*, 2020, **22**, 7169-7192.
8. W. Humphrey, A. Dalke and K. Schulten, *J. Mol. Graph.*, 1996, **14**, 33-38.
9. M. J. Frisch, G. W. Trucks, H. B. Schlegel, G. E. Scuseria, M. A. Robb, J. R. Cheeseman, G. Scalmani, V. Barone, G. A. Petersson, H. Nakatsuji, X. Li, M. Caricato, A. V. Marenich, J. Bloino, B. G. Janesko, R. Gomperts, B. Mennucci, H. P. Hratchian, J. V. Ortiz, A. F. Izmaylov, J. L. Sonnenberg, Williams, F. Ding, F. Lipparini, F. Egidi, J. Goings, B. Peng, A. Petrone, T. Henderson, D. Ranasinghe, V. G. Zakrzewski, J. Gao, N. Rega, G. Zheng, W. Liang, M. Hada, M. Ehara, K. Toyota, R. Fukuda, J. Hasegawa, M. Ishida, T. Nakajima, Y. Honda, O. Kitao, H. Nakai, T. Vreven, K. Throssell, J. A. Montgomery Jr., J. E. Peralta, F. Ogliaro, M. J. Bearpark, J. J. Heyd, E. N. Brothers, K. N. Kudin, V. N. Staroverov, T. A. Keith, R. Kobayashi, J. Normand, K. Raghavachari, A. P. Rendell, J. C. Burant, S. S. Iyengar, J. Tomasi, M. Cossi, J. M. Millam, M. Klene, C. Adamo, R. Cammi, J. W. Ochterski, R. L. Martin, K. Morokuma, O. Farkas, J. B. Foresman and D. J. Fox, *Gaussian 16 Rev. C.01*, Gaussian, Inc., Wallingford CT, 2016.
10. M. J. Frisch, G. W. Trucks, H. B. Schlegel, G. E. Scuseria, M. A. Robb, J. R. Cheeseman, G. Scalmani, V. Barone, G. A. Petersson, H. Nakatsuji, X. Li, M. Caricato, A. V. Marenich, J. Bloino, B. G. Janesko, R. Gomperts, B. Mennucci, H. P. Hratchian, J. V. Ortiz, A. F. Izmaylov, J. L. Sonnenberg, Williams, F. Ding, F. Lipparini, F. Egidi, J. Goings, B. Peng, A. Petrone, T. Henderson, D. Ranasinghe, V. G. Zakrzewski, J. Gao, N. Rega, G. Zheng, W. Liang, M. Hada, M. Ehara, K. Toyota, R. Fukuda, J. Hasegawa, M. Ishida, T. Nakajima, Y. Honda, O. Kitao, H. Nakai, T. Vreven, K. Throssell, J. A. Montgomery Jr., J. E. Peralta, F. Ogliaro, M. J. Bearpark, J. J. Heyd, E. N. Brothers, K. N. Kudin, V. N. Staroverov, T. A. Keith, R. Kobayashi, J. Normand, K. Raghavachari, A. P. Rendell, J. C. Burant, S. S. Iyengar, J. Tomasi, M. Cossi, J. M. Millam, M. Klene, C. Adamo, R. Cammi, J. W. Ochterski, R. L. Martin, K. Morokuma, O. Farkas, J. B. Foresman and D. J. Fox, *Gaussian 16 Rev. C.02*, Gaussian, Inc., Wallingford CT, 2016.
11. J.-D. Chai and M. Head-Gordon, *Phys. Chem. Chem. Phys.*, 2008, **10**, 6615-6620.
12. R. Ditchfield, W. J. Hehre and J. A. Pople, *J. Chem. Phys.*, 1971, **54**, 724-728.
13. W. J. Hehre, R. Ditchfield and J. A. Pople, *J. Chem. Phys.*, 1972, **56**, 2257-2261.
14. M. M. Francl, W. J. Pietro, W. J. Hehre, J. S. Binkley, M. S. Gordon, D. J. DeFrees and J. A. Pople, *J. Chem. Phys.*, 1982, **77**, 3654-3665.

15. V. A. Rassolov, J. A. Pople, M. A. Ratner and T. L. Windus, *J. Chem. Phys.*, 1998, **109**, 1223-1229.
16. F. Weigend and R. Ahlrichs, *Phys. Chem. Chem. Phys.*, 2005, **7**, 3297-3305.
17. F. Weigend, *Phys. Chem. Chem. Phys.*, 2006, **8**, 1057-1065.
18. V. Barone and M. Cossi, *J. Phys. Chem. A.*, 1998, **102**, 1995-2001.
19. M. Cossi, N. Rega, G. Scalmani and V. Barone, *J. Comput. Chem.*, 2003, **24**, 669-681.
20. H. W. Horn, G. O. Jones, D. S. Wei, K. Fukushima, J. M. Lecuyer, D. J. Coady, J. L. Hedrick and J. E. Rice, *J. Phys. Chem. A.*, 2012, **116**, 12389-12398.
21. R. F. Ribeiro, A. V. Marenich, C. J. Cramer and D. G. Truhlar, *J. Phys. Chem. B.*, 2011, **115**, 14556-14562.
22. Y.-P. Li, J. Gomes, S. Mallikarjun Sharada, A. T. Bell and M. Head-Gordon, *J. Phys. Chem. C.*, 2015, **119**, 1840-1850.
23. G. Luchini, J. V. Alegre-Requena, I. Funes-Ardoiz and R. S. Paton, *F1000Research*, 2020, **9**, 291.
24. C. Y. Legault, *CYLview, 1.0b*, Université de Sherbrooke, 2009, http://www.cylview.org.